Reduced Order Model Feedback Control Design: Computational Studies for Thin Cylindrical Shells [1]

H.T. Banks R.C.H. del Rosario R.C. Smith

Center for Research in Scientific Computation
North Carolina State University
Raleigh, NC 27695

Abstract

Reduced order models employing the Lagrange and POD reduced basis methods in numerical approximation and feedback control of systems are presented and numerically tested. The system considered is a thin cylindrical shell with surface-mounted piezoceramic actuators. Donnell-Mushtari equations, modified to include Kelvin-Voigt damping, are used to model the system dynamics. Basis functions constructed from Fourier polynomials tensored with cubic splines are employed in the Galerkin expansion of the full order model. Reduced basis elements are then formed from full order approximations of the exogenously excited shell taken at different time instances. Numerical examples illustrating the features of the reduced basis methods are presented. To investigate the behavior of the methods when executed on physical systems, the numerical implementation of reduced order control gains in the full order model is developed and numerical examples are presented.

[1]Research supported in part by the U.S. Air Force Office of Scientific Research under grants AFSOR F49620-95-1-0236 and AFSOR F49620-98-1-0180

1 Introduction

There is a vast and growing literature on the design of feedback control laws based on partial differential equation (PDE) models for physical systems. Much of the attention has been on theory – for a partial summary see Chapter 7 of [4] and the references cited therein. More recently, efforts to experimentally implement the theoretical ideas from feedback control theory has provided additional stimulus for the development of efficient computation methodologies. In [4, Chapter 8],[6], investigators succeeded in experimentally implementing PDE-based feedback controls and compensators on a simple physical system involving a thin plate, obtaining remarkable control authority in the context of smart material technologies (in particular, piezoceramic sensing and actuation). The efforts involve real time computationally intensive algorithms which are unlikely to be extended to more complex physical arenas such as shells [9, 10, 11] and structural acoustic systems [5] if the computations are based on usual finite element methods for full-order, physically accurate PDE models. Thus, the success of future efforts in the direction of PDE-based control and compensator design clearly rests in the development of reduced order model (ROM) based calculations for use in on-line, real-time methodologies. This note offers a first step in that direction.

We present here some initial computational findings for ROM feedback control design using two distinct but related approaches: (i) the so-called reduced basis methods (RBM) of Lagrange, Taylor and Hermite type and (ii) the (perhaps too) popular proper orthogonal decomposition (POD) methods that are generally attributed to Karhunen and Loève. Our findings, some of which are detailed below and summarized in the concluding section, suggest that in some cases one or the other of the RBM/POD based computational approaches might prove useful in real time implementation of feedback control/compensator design.

The RBM ideas appear to have their origins in the suggestions of Almroth [1] and Nagy [17] which were developed by Noor and colleagues [18, 19, 20] in the context of simulations for structures and later by Peterson [21] in high Reynolds numbers incompressible viscous flow simulations. The first use of RBM methods for open loop control of fluids as described by Navier Stokes type PDE can be found in [12, 13]. Roughly speaking, the RBM employs parameter-dependent solutions of the system to be approximated. These solutions are used to construct basis elements in the hope that solutions at other parameter values can be represented in terms of perturbations of solutions given at carefully chosen parameter values (the Lagrange basis approach) or in terms of a "moving frame" (the Taylor approach).

The POD or Karhunen-Loève methods begin with essentially the same information (solutions of the system – as in RBM these can be experimental or computational) about the full order system to be approximated. Through an orthogonalization procedure, one then attempts to extract characteristic information from the solution set and represent this in an "optimal" way in constructing a reduced set of basis elements.

The efforts of Lumley [15], (see also the review in [7]) have stimulated significant research into the use of POD methods in simulations in fluid mechanics (especially turbulence and coherent structures) as well as in image processing and signal analysis among others (again see [7] and the references therein). The successful use of POD in open loop control problems [16] is very recent.

We discuss here (for the first time to our knowledge) the use of RBM and POD as applied to PDE-based feedback control design. As the reader will see, these methods are not offered

as a panacea – they must be used with care and even then may not prove adequate in all regimes. Our goals are to provide a preliminary investigation into what, if any, advantages these approaches can provide to the area of feedback control design for complex physical systems. We chose to do to this in the context of piezoceramic-actuated cylindrical shell vibrations. This shell paradigm is not an essential feature of our investigations – it does provide a convenient 2-D example for which the full order calculations most likely will, without special efforts, prohibit feedback control design in current on-line computational environments. It is also a model for which we have some computational experience. The ideas we discuss below should be readily applicable to plates and other structures, structural acoustic systems and more general fluid/structure interaction systems.

In Section 2, we summarize the shell model as developed elsewhere and then discuss briefly general finite dimensional approximations in Section 3. The ideas behind the RBM of Lagrange and Hermite type are given in Section 4 and then the performance of Lagrange elements is illustrated. The next section presents use of POD design in the same example. In Sections 4 and 5 the ROM control designs are applied to the ROM system, which is not what one must do in actual applications. To gain better insight into the performance of the ideas in applications we present in Section 6 a discussion of the use of the reduced order designed gains in the full order system.

2 PDE Model

The system we consider in this paper is a cylindrical shell with surface-mounted piezoceramic patches as actuators. In Figure 1, we indicate the longitudinal (u), circumferential (v) and transverse (w) displacements of the middle surface. The physical properties of the shell are denoted by the length ℓ, thickness h, radius R, density ρ, Young's modulus E, Poisson ratio ν and Kelvin-Voigt damping coefficient c_D. As with common experimental setups, we model clamped edges for the shell. Hence the longitudinal, circumferential and transverse displacements at the edges along with transverse slopes are assumed to be fixed.

Also portrayed in Figure 1 are the locations of the s pairs of surface-mounted piezoceramic patches which can be used as sensors and/or actuators in vibration suppression applications. The center of the i^{th} patch pair is denoted by $(\bar{x}_i, \bar{\theta}_i)$ and the edges are designated by $x_{i1}, x_{2i}, \theta_{1i}, \theta_{2i}$. Currently, only the actuating capabilities of the piezoceramic patches coming from material deformations in response to applied voltages are incorporated in the model but extensions could be readily made to include the sensing capabilities of the patches. For simplicity in the exposition, the patches are all assumed to have thickness h_{pe}, Young's modulus E_{pe}, Poisson ratio ν_{pe} and Kelvin-Voigt damping coefficient c_{Dpe}. It is also assumed that the glue bonding layer provides negligible contribution to the structural dynamics, and the passive patch contributions in the density, moment, and force resultants are neglected. Discussions regarding the incorporation of differing patch characteristics and bonding layers in the model could be found in [2, 4], and for the system including passive patch contributions, the reader is referred to [4, 11].

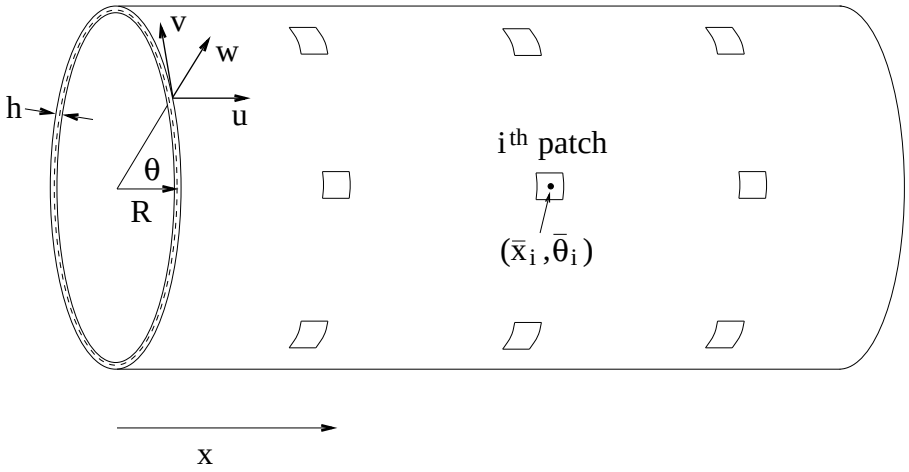

Figure 1. Thin cylindrical shell with surface mounted piezoceramic patches.

The strong form of the Donnell-Mushtari equations obtained by moment and force balancing detailed in [4, 14] is given by

$$
\begin{aligned}
&R\rho h\frac{\partial^2 u}{\partial t^2} - R\frac{\partial N_x}{\partial x} - \frac{\partial N_{\theta x}}{\partial \theta} = R\hat{q}_x - R\sum_{i=1}^{s}\frac{\partial (N_x)_{pe_i}}{\partial x}\mathcal{S}_{pe_i}(x,\theta)\\
&R\rho h\frac{\partial^2 v}{\partial t^2} - \frac{\partial N_\theta}{\partial \theta} - R\frac{N_{x\theta}}{\partial x} = R\hat{q}_\theta - \sum_{i=1}^{s}\frac{\partial (N_\theta)_{pe_i}}{\partial \theta}\mathcal{S}_{pe_i}(x,\theta)\\
&R\rho h\frac{\partial^2 w}{\partial t^2} - R\frac{\partial^2 M_x}{\partial x^2} - \frac{1}{R}\frac{\partial^2 M_\theta}{\partial \theta^2} - 2\frac{\partial^2 M_{x\theta}}{\partial x \partial \theta} + N_\theta\\
&\qquad\qquad = R\hat{q}_n - \sum_{i=1}^{s}\left[R\frac{\partial^2 (M_x)_{pe_i}}{\partial x^2} + \frac{1}{R}\frac{\partial^2 (M_\theta)_{pe_i}}{\partial \theta^2}\right].
\end{aligned}
\tag{1}
$$

In these equations, $M_x, M_\theta, M_{\theta x}$ and $M_{x\theta}$ are internal moments while $N_x, N_\theta, N_{\theta x}$ and $N_{x\theta}$ denote internal force resultants. The functions $\hat{q}_x, \hat{q}_\theta, \hat{q}_n$ are used to model external surface forces while the external moments and forces generated by the i^{th} patch pair are denoted by $(M_x)_{pe_i}, (M_\theta)_{pe_i}, (N_x)_{pe_i}, (N_\theta)_{pe_i}$. The indicator function $\mathcal{S}_{pe_i}(x,\theta) = S_{1,2}(x)\hat{S}_{1,2}(\theta)$, is used to describe the opposite direction of the forces at points symmetric to the center $(\bar{x}_i, \bar{\theta}_i)$ of the i^{th} patch (which are induced when voltage is applied to the patches). Here

$$
S_{1,2}(x) = \begin{cases} 1 & , \quad x < (x_{1i}+x_{2i})/2 \\ 0 & , \quad x = (x_{1i}+x_{2i})/2 \\ -1 & , \quad x > (x_{1i}+x_{2i})/2 \end{cases}, \quad \hat{S}_{1,2}(\theta) = \begin{cases} 1 & , \quad \theta < (\theta_{1i}+\theta_{2i})/2 \\ 0 & , \quad \theta = (\theta_{1i}+\theta_{2i})/2 \\ -1 & , \quad \theta > (\theta_{1i}+\theta_{2i})/2 \end{cases}.
$$

Under the assumption that stress is proportional to a linear combination of strain and strain rate, the expressions for the internal force and moment resultants are derived in [2, 4]

yielding a model which incorporates Kelvin-Voigt or strong internal damping. The resultants derived this way are given by

$$
\begin{aligned}
N_x &= \frac{Eh}{(1-\nu^2)}\left[\frac{\partial u}{\partial x}+\nu\left(\frac{1}{R}\frac{\partial v}{\partial \theta}+\frac{w}{R}\right)\right]+\frac{c_D h}{(1-\nu^2)}\frac{\partial}{\partial t}\left[\frac{\partial u}{\partial x}+\nu\left(\frac{1}{R}\frac{\partial v}{\partial \theta}+\frac{w}{R}\right)\right]\\
N_\theta &= \frac{Eh}{(1-\nu^2)}\left[\frac{1}{R}\frac{\partial v}{\partial \theta}+\frac{w}{R}+\nu\frac{\partial u}{\partial x}\right]+\frac{c_D h}{(1-\nu^2)}\frac{\partial}{\partial t}\left[\frac{1}{R}\frac{\partial v}{\partial \theta}+\frac{w}{R}+\nu\frac{\partial u}{\partial x}\right]\\
N_{x\theta} = N_{\theta x} &= \frac{Eh}{2(1+\nu)}\left[\frac{\partial v}{\partial x}+\frac{1}{R}\frac{\partial u}{\partial \theta}\right]+\frac{c_D h}{2(1+\nu)}\frac{\partial}{\partial t}\left[\frac{\partial v}{\partial x}+\frac{1}{R}\frac{\partial u}{\partial \theta}\right]\\
M_x &= -\frac{Eh^3}{12(1-\nu^2)}\left[\frac{\partial^2 w}{\partial x^2}+\frac{\nu}{R^2}\frac{\partial^2 w}{\partial \theta^2}\right]-\frac{c_D h^3}{12(1-\nu^2)}\frac{\partial}{\partial t}\left[\frac{\partial^2 w}{\partial x^2}+\frac{\nu}{R^2}\frac{\partial^2 w}{\partial \theta^2}\right]\\
M_\theta &= -\frac{Eh^3}{12(1-\nu^2)}\left[\frac{1}{R^2}\frac{\partial^2 w}{\partial \theta^2}+\nu\frac{\partial^2 w}{\partial x^2}\right]-\frac{c_D h^3}{12(1-\nu^2)}\frac{\partial}{\partial t}\left[\frac{1}{R^2}\frac{\partial^2 w}{\partial \theta^2}+\nu\frac{\partial^2 w}{\partial x^2}\right]\\
M_{x\theta} = M_{\theta x} &= -\frac{Eh^3}{12R(1+\nu)}\frac{\partial^2 w}{\partial x\partial \theta}-\frac{c_D h^3}{12R(1+\nu)}\frac{\partial}{\partial t}\left[\frac{\partial^2 w}{\partial x\partial \theta}\right].
\end{aligned}
\tag{2}
$$

The substitution of these equations in (1) yields the damped form of the Donnell-Mushtari equations. If the terms with damping coefficient c_D are dropped in (2), the regular Donnell-Mushtari equations are formed.

The external resultants are derived under the assumption that the strain generated by a patch is proportional to the applied voltage (see [2]). This constant of proportionality (assumed uniform for all the patches) will be denoted by d_{31}. The model allows differing voltage inputs to the outer and inner patches of the i^{th} patch pair. Denoting the outer and inner induced voltages by $V_{i1}(t)$ and $V_{i2}(t)$, respectively, we take the total external moments and forces generated by the i^{th} patch to be

$$
\begin{aligned}
(M_x)_{pe_i} &= \frac{-E_{pe}d_{31}}{(1-\nu_{pe})h_{pe}}\left[\left(\frac{a_2}{2}+\frac{a_3}{3R}\right)V_{i1}-\left(\frac{a_2}{2}-\frac{a_3}{3R}\right)V_{i2}\right]\chi_{pe_i}(x,\theta)\\
(M_\theta)_{pe_i} &= \frac{-E_{pe}d_{31}a_2}{2(1-\nu_{pe})h_{pe}}\left[V_{i1}-V_{i2}\right]\chi_{pe_i}(x,\theta)\\
(N_x)_{pe_i} &= \frac{-E_{pe}d_{31}}{(1-\nu_{pe})h_{pe}}\left[\left(h_{pe}+\frac{a_2}{2R}\right)V_{i1}+\left(h_{pe}-\frac{a_2}{2R}\right)V_{i2}\right]\mathcal{S}_{pe_i}(x,\theta)\chi_{pe_i}(x,\theta)\\
(N_\theta)_{pe_i} &= \frac{-E_{pe}}{1-\nu_{pe}}d_{31}[V_{i1}-V_{i2}]\mathcal{S}_{pe_i}(x,\theta)\chi_{pe_i}(x,\theta)
\end{aligned}
\tag{3}
$$

where the constants $a_2=(h/2+h_{pe})^2-h^2/4$ and $a_3=(h/2+h_{pe})^3-h^3/8$ arise from integrating through the thickness of the patch. The characteristic functions $\chi_{pe_i}(x,\theta)$ have definition

$$
\chi_{pe_i}(x,\theta)=\begin{cases}1\ , & x_{i1}\le x\le x_{i2},\ \theta_{i1}\le x\le\theta_{i2}\\ 0\ , & \text{otherwise}\ ,\end{cases}
\tag{4}
$$

where $x_{i1}, x_{i2}, \theta_{i1}, \theta_{i2}$ are the edge coordinates of the i^{th} patch.

The weak form of the equations (1) as derived in [4] has the form

$$\begin{aligned}
\int_{\Gamma_0} \left\{ R\rho h \frac{\partial^2 u}{\partial t^2}\eta_1 + RN_x \frac{\partial \eta_1}{\partial x} + N_{\theta x}\frac{\partial \eta_1}{\partial \theta} - R\hat{q}_x \eta_1 - R\sum_{i=1}^{s}(N_x)_{pe_i}\frac{\partial \eta_1}{\partial x} \right\} d\gamma &= 0 \\
\int_{\Gamma_0} \left\{ R\rho h \frac{\partial^2 v}{\partial t^2}\eta_2 + N_\theta \frac{\partial \eta_2}{\partial \theta} + RN_{x\theta}\frac{\partial \eta_2}{\partial x} - R\hat{q}_\theta \eta_2 - \sum_{i=1}^{s}(N_\theta)_{pe_i}\frac{\partial \eta_2}{\partial \theta} \right\} d\gamma &= 0 \\
\int_{\Gamma_0} \left\{ R\rho h \frac{\partial^2 w}{\partial t^2}\eta_3 + N_\theta \eta_3 - RM_x \frac{\partial^2 \eta_3}{\partial x^2} - \frac{1}{R}M_\theta \frac{\partial^2 \eta_3}{\partial \theta^2} - 2M_{x\theta}\frac{\partial^2 \eta_3}{\partial x \partial \theta} \right. & \\
\left. -R\hat{q}_n \eta_3 + \sum_{i=1}^{s}\left[R(M_x)_{pe_i}\frac{\partial^2 \eta_3}{\partial x^2} + \frac{1}{R}(M_\theta)_{pe_i}\frac{\partial^2 \eta_3}{\partial \theta^2} \right] \right\} d\gamma &= 0
\end{aligned} \tag{5}$$

for all test functions $\Psi = (\eta_1, \eta_2, \eta_3)$. Here Γ_0 denotes the region occupied by the middle surface of the shell, i.e., $\Gamma_0 = \{(x, \theta) : 0 \le x \le \ell, 0 \le \theta \le 2\pi\}$. The state variables for the problem in second-order form are taken to be $y = (u, v, w)$ in the state space

$$H = L^2(\Gamma_0) \times L^2(\Gamma_0) \times L^2(\Gamma_0) \ .$$

Coupled to the system (5) are the fixed-edge boundary conditions

$$u(t,0,\theta) = u(t,\ell,\theta) = v(t,0,\theta) = v(t,\ell,\theta) = 0 \tag{6a}$$

$$w(t,0,\theta) = w(t,\ell,\theta) = \frac{\partial w(t,0,\theta)}{\partial x} = \frac{\partial w(t,\ell,\theta)}{\partial x} = 0 \tag{6b}$$

Test functions are chosen to satisfy smoothness criteria and the boundary conditions, and we take

$$V = H_0^1(\Gamma_0) \times H_0^1(\Gamma_0) \times H_0^2(\Gamma_0) \ , \tag{7}$$

where

$$H_0^1(\Gamma_0) = \left\{ \eta \in H^1(\Gamma_0) : \eta(0,\cdot) = \eta(\ell,\cdot) = 0 \right\}$$

$$H_0^2(\Gamma_0) = \left\{ \eta \in H^2(\Gamma_0) : \eta(0,\cdot) = \frac{\partial \eta(0,\cdot)}{\partial x} = \eta(\ell,\cdot) = \frac{\partial \eta(\ell,\cdot)}{\partial x} = 0 \right\}.$$

3 Finite Dimensional Approximation

To approximate the solutions u, v and w to the system (5), we choose basis functions $\{\mathcal{B}_{u_i}\}_{i=1}^{\mathcal{N}_u}$, $\{\mathcal{B}_{v_i}\}_{i=1}^{\mathcal{N}_v}$ and $\{\mathcal{B}_{w_i}\}_{i=1}^{\mathcal{N}_w}$ spanning a finite dimensional approximating subspace $V^{\mathcal{N}} \subset V$, i.e.,

$$V^{\mathcal{N}} = \text{span}\{\mathcal{B}_{u_i}\}_{i=1}^{\mathcal{N}_u} \times \text{span}\{\mathcal{B}_{v_i}\}_{i=1}^{\mathcal{N}_v} \times \text{span}\{\mathcal{B}_{w_i}\}_{i=1}^{\mathcal{N}_w} \tag{8}$$

to form the Galerkin expansions

$$y^{\mathcal{N}}(t,x,\theta) = \begin{bmatrix} u^{\mathcal{N}}(t,x,\theta) \\ v^{\mathcal{N}}(t,x,\theta) \\ w^{\mathcal{N}}(t,x,\theta) \end{bmatrix} = \begin{bmatrix} \sum_{i=1}^{\mathcal{N}_u} u_i(t)\mathcal{B}_{u_i}(x,\theta) \\ \sum_{i=1}^{\mathcal{N}_v} v_i(t)\mathcal{B}_{v_i}(x,\theta) \\ \sum_{i=1}^{\mathcal{N}_w} w_i(t)\mathcal{B}_{w_i}(x,\theta) \end{bmatrix} . \tag{9}$$

Then $V^{\mathcal{N}}$ has dimension $\mathcal{N} = \mathcal{N}_u + \mathcal{N}_v + \mathcal{N}_w$. We denote the use of standard basis functions such as cubic or linear splines by "full order discretization" while "reduced basis methods" denote the use of a smaller approximating subspace. The reduced basis spaces we consider in the next section are subspaces of the full order finite element subspace.

The approximating system is determined by restricting the weak form (5) to $V^{\mathcal{N}}$ with basis functions used as test functions. This is equivalent to orthogonalizing the residual with respect to elements from $V^{\mathcal{N}}$. To write the system in first order form, we consolidate the generalized coefficients $u_i(t), v_i(t)$ and $w_i(t)$ into one vector

$$\vartheta^{\mathcal{N}}(t) = [u_1(t), \ldots, u_{\mathcal{N}_u}(t), v_1(t), \ldots, v_{\mathcal{N}_v}(t), w_1(t), \ldots, w_{\mathcal{N}_w}(t)]^T \in \mathbb{R}^{\mathcal{N}} .$$

The resulting matrix system is then given by

$$\begin{bmatrix} K_E^{\mathcal{N}} & 0 \\ 0 & M^{\mathcal{N}} \end{bmatrix} \begin{bmatrix} \dot{\vartheta}^{\mathcal{N}}(t) \\ \ddot{\vartheta}^{\mathcal{N}}(t) \end{bmatrix} = \begin{bmatrix} 0 & K_E^{\mathcal{N}} \\ -K_E^{\mathcal{N}} & -K_{C_D}^{\mathcal{N}} \end{bmatrix} \begin{bmatrix} \vartheta^{\mathcal{N}}(t) \\ \dot{\vartheta}^{\mathcal{N}}(t) \end{bmatrix} + \begin{bmatrix} 0 \\ \hat{B}^{\mathcal{N}} \end{bmatrix} U(t) + \begin{bmatrix} 0 \\ \hat{F}^{\mathcal{N}}(t) \end{bmatrix}$$
$$\begin{bmatrix} K_E^{\mathcal{N}} & 0 \\ 0 & M^{\mathcal{N}} \end{bmatrix} \begin{bmatrix} \vartheta^{\mathcal{N}}(0) \\ \dot{\vartheta}^{\mathcal{N}}(0) \end{bmatrix} = \begin{bmatrix} y_1^{\mathcal{N}} \\ y_2^{\mathcal{N}} \end{bmatrix} , \tag{10}$$

where the control input vector $U(t)$ has elements

$$U(t) = [V_{11}(t), V_{12}(t), \ldots, V_{i1}(t), V_{i2}(t), \ldots V_{s1}(t), V_{s2}(t)]^T \in \mathbb{R}^{2s} .$$

The reader is referred to Section 4.4 of [9] for details concerning the creation of the matrices $K_E^{\mathcal{N}}, M^{\mathcal{N}}, K_{C_D}^{\mathcal{N}}, \hat{B}^{\mathcal{N}}$ and $\hat{F}^{\mathcal{N}}$. To write the system in a form suitable for simulations, parameter estimation and control applications, we invert the mass matrix to yield a Cauchy equation of the form

$$\begin{aligned} \dot{z}^{2\mathcal{N}}(t) &= A^{2\mathcal{N}} z^{2\mathcal{N}}(t) + B^{2\mathcal{N}} U(t) + G^{2\mathcal{N}}(t) \\ z^{2\mathcal{N}}(0) &= z_0^{2\mathcal{N}} , \end{aligned} \tag{11}$$

where $z^{2\mathcal{N}}(t) = [\vartheta^{\mathcal{N}}(t), \dot{\vartheta}^{\mathcal{N}}(t)] \in \mathbb{R}^{2\mathcal{N}}$.

The discretization method using full order basis elements employing cubic splines in the x-direction and Fourier polynomials in the circumferential direction was investigated in [9], [10] and [11]. Examples illustrating quadratic rate of convergence were given, and the flexibility of the method in adapting to different boundary conditions was demonstrated. For the rest of this paper, full order basis functions in the u, v and w directions will be denoted by $\mathcal{B}_{u_i}, \mathcal{B}_{v_i}$ and $\mathcal{B}_{w_i}$, respectively and the dimension of the full order finite element subspace $V^{\mathcal{N}}$ will be denoted by $\mathcal{N}$, where $\mathcal{N} = \mathcal{N}_u + \mathcal{N}_v + \mathcal{N}_w$.

4 The Reduced Basis Method

Full order discretizations result in system matrices with large dimension and hence are not readily implementable in real time computation. As shown in [11], a large number of basis functions was needed to resolve the system (11), where $\mathcal{N}_u = \mathcal{N}_v = 117$ and $\mathcal{N}_w = 99$ basis functions were used for a total of $2\mathcal{N} = 666$ coefficients in the ODE system (11). Thus, the investigation of model reduction techniques is a necessary next step in this study.

The method we investigate involves the use of a reduced basis subspace to approximate the displacements u, v and w. Three ways to choose the reduced basis subspaces were discussed in [12], namely the Taylor, the Lagrange and the Hermite reduced basis methods. In this section, we illustrate the use of Lagrange and Hermite subspaces in shell applications, and give examples illustrating implementation of the Lagrange subspace which in this paper we will call the *reduced basis method*.

The basis elements in the Lagrange subspace are snapshots (i.e., solutions evaluated at N_R times $\{t_1, \ldots t_{N_R}\}$) of the model obtained by solving the system (5) using a full order method. If experimental data is available, measurements of the displacements could also be used as reduced basis elements. Letting Υ_{u_i}, Υ_{v_i} and Υ_{w_i}, $i = 1, \ldots, N_R$, denote the snapshots in the u, v and w directions, respectively, the resulting reduced order space denoted by $V^{\mathcal{N}_R}$ is then expressed as

$$V^{\mathcal{N}_R} = \text{span}\left\{\Upsilon_{u_i}\right\}_{i=1}^{N_R} \times \text{span}\left\{\Upsilon_{v_i}\right\}_{i=1}^{N_R} \times \text{span}\left\{\Upsilon_{w_i}\right\}_{i=1}^{N_R} \ . \tag{12}$$

Since $(\Upsilon_{u_i}, \Upsilon_{v_i}, \Upsilon_{w_i}) \in V^{\mathcal{N}}$, $i = 1, \ldots, N_R$, and the reduced basis subspace $V^{\mathcal{N}_R}$ is in the span of the Υ's, then $V^{\mathcal{N}_R} \subset V^{\mathcal{N}}$. Note that the dimension of $V^{\mathcal{N}_R}$ is $3N_R$ which we denote from now on by $\mathcal{N}_R$.

As an alternative approach, the Hermite subspace could be formed by taking as basis elements the full order solutions and their first derivatives at $N_R/2$ times. This gives us the subspace

$$V^{\mathcal{N}_R} = \text{span}\left\{\Upsilon_{u_i}, \dot{\Upsilon}_{u_i}\right\}_{i=1}^{N_R/2} \times \text{span}\left\{\Upsilon_{v_i}, \dot{\Upsilon}_{v_i}\right\}_{i=1}^{N_R/2} \times \text{span}\left\{\Upsilon_{w_i}, \dot{\Upsilon}_{w_i}\right\}_{i=1}^{N_R/2}$$

with dimension $\mathcal{N}_R = 3N_R$.

Once we have formed a reduced order basis, the displacements u, v and w are discretized using the reduced basis functions $\Upsilon_{u_i}, \Upsilon_{v_i}, \Upsilon_{w_i}$. The weak form (5) is restricted to the reduced basis space $V^{\mathcal{N}_R}$ and the first order Cauchy equation (11) of dimension $2\mathcal{N}_R$ is now given by

$$\begin{aligned} \dot{z}^{2\mathcal{N}_R}(t) &= A^{2\mathcal{N}_R} z^{2\mathcal{N}_R}(t) + B^{2\mathcal{N}_R} U(t) + G^{2\mathcal{N}_R}(t) \\ z^{2\mathcal{N}_R}(0) &= z_0^{2\mathcal{N}_R} \ , \end{aligned} \tag{13}$$

where $z^{2\mathcal{N}_R}(t) \in \mathbb{R}^{2\mathcal{N}_R}$ now contains the coefficients in the reduced order approximations.

4.1 Numerical Examples

We illustrate use of the Lagrange reduced basis method through two numerical examples. An uncontrolled shell with periodic external excitation was numerically simulated to compare the performance of the reduced basis method with the full order method. Then an LQR control design using the reduced basis functions was applied to a shell excited by the same periodic external force.

4.1.1 Uncontrolled Shell Model with Periodic Exogenous Input

To model a periodic noise source localized near the axial shell center ($x = \ell/2$) and at $\theta = 0$ and $\theta = \pi$, we consider an external force of the form

$$\begin{aligned} \hat{q}_x(x,\theta,t) &= \frac{1}{100} e^{-20(x-\ell/2)^2} \Theta(\theta) g(t) \\ \hat{q}_\theta(x,\theta,t) &= 0 \\ \hat{q}_\eta(x,\theta,t) &= e^{-20(x-\ell/2)^2} \Theta(\theta) g(t) \ , \end{aligned} \tag{14}$$

where

$$\Theta(\theta) = \begin{cases} 1 - e^{-(\theta-\pi/2)^6/2} & , \quad 0 \le \theta < \pi \\ 1 - e^{-(\theta-3\pi/2)^6/2} & , \quad \pi \le \theta < 2\pi \end{cases} \ , \tag{15}$$

and $g(t) = \sin(1000\pi t)$. The spatial components of this force, i.e., the axial and circumferential components, are illustrated in Figure 2.

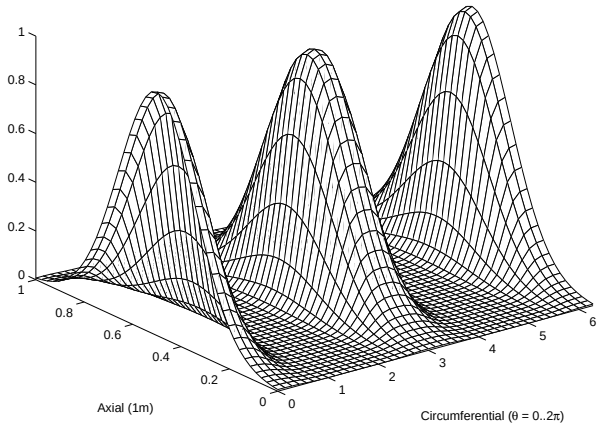

Figure 2. Spatial distribution of transverse and longitudinal forces (14) to the shell.

For the full order discretization, a Galerkin expansion using cubic splines tensored with Fourier polynomials as basis functions was used to discretize the longitudinal, circumferential and transverse displacements. As illustrated in [9], the cubic splines along the x-axis are created by first partitioning the interval $[0, \ell]$ into N uniform partitions. As usual, $N+3$ standard cubic splines arise from the partitions and these are modified to satisfy the boundary conditions being considered in the model. In this report, the clamped edge boundary conditions (6a) enforce zero displacements at the boundaries for the longitudinal and circumferential directions, i.e., $u(t,0,\theta) = u(t,\ell,\theta) = v(t,0,\theta) = v(t,\ell,\theta) = 0$. Modification of the standard cubic splines to satisfy these conditions results in $N+1$ modified elements to be used as basis elements. We lose two more degrees of freedom in the transverse direction to satisfy the additional zero slope condition (6b), i.e., $w(t,0,\theta) = w(t,\ell,\theta) = \partial w(t,0,\theta)/\partial x = \partial w(t,\ell,\theta)/\partial x = 0$. Hence $N-1$ modified cubic spline elements are formed as basis elements in the w direction. A Fourier index M gives rise to $2M+1$ Fourier components given by $\sin(M\theta), \ldots, \sin(\theta), 1, \cos(\theta), \ldots, \cos(M\theta)$.

In previous full order computations (see [11]), the discretization sizes $N = 12$ and $M = 4$ were needed to fully approximate the closed loop system. This resulted in the following number of basis functions: $\mathcal{N}_u = \mathcal{N}_v = 13(2 \times 4 + 1) = 117$ and $\mathcal{N}_w = 11(2 \times 4 + 1) = 99$, for a total of $\mathcal{N} = 333$ basis elements in the second order system and $2\mathcal{N} = 666$ coefficients in the first order reformulation (11).

The dimensions and material properties of the shell being modeled, consistent with those used in previous computational experiments are summarized in Table 1. This is done to allow comparison with the control results for the full order model discretization given in [10, 11].

To create the Lagrange subspace, we obtain realizations of the model using the full order discretization at N_R time instances between $t = 0$ and $t = 0.1$ sec. The reduced order model was discretized using $N_R = 1, 2, 3, 4$ (hence $\mathcal{N}_R = 3, 6, 9, 12$) to determine if the approximation becomes more accurate as more basis functions are employed.

The time histories at the point p_1 with coordinates $(\hat{x}, \hat{\theta}) = (3\ell/4, \pi/4)$ using $N_R = 1$ ($\mathcal{N}_R = 3$ total basis functions) together with full order model displacements (with $\mathcal{N} = 333$) at the same point are presented in Figure 3. The figure clearly shows that the system is not resolved, i.e., not well approximated, with 3 basis functions. Numerical results using $\mathcal{N}_R = 6$ and 9 basis functions ($N_R = 2$ and 3) are reported in Figure 4 where the *difference* between the full order and reduced order trajectories at p_1 are plotted. It can be seen from the error plots that we get a good approximation with 9 basis functions in which we obtain a reduction from 333 basis functions to 9 basis functions, with a corresponding reduction in the size of the finite dimensional system (11) from 666 to 18. Since the difference between full and reduced order approximations with 12 basis functions is at the same level as 9 basis functions, the plots are not given here. We point out that scales in the u, v and w directions (in Figures 3 and 4) are not uniform due to the differing magnitudes of external forces acting on the shell resulting in different magnitude displacements for the three directions.

To quantify the performance of the reduced basis methods, we use the ℓ_1 norm of the difference between the full order and reduced order displacements. This is obtained by first taking 500 full and reduced order point displacements at p_1 between $t = 0$ and $t = 0.1$ and computing the error, for example, in the longitudinal direction u, using

$$\|u^{\mathcal{N}}(\cdot, \hat{x}, \hat{\theta}) - u^{\mathcal{N}_R}(\cdot, \hat{x}, \hat{\theta}\|_{\ell_1} = \sum_{i=1}^{500} \left| u^{\mathcal{N}}(t_i, \hat{x}, \hat{\theta}) - u^{\mathcal{N}_R}(t_i, \hat{x}, \hat{\theta}) \right| \ ,$$

where $u^{\mathcal{N}}$ is the full order approximation and $u^{\mathcal{N}_R}$ is the reduced order approximation. The ℓ_1 norm of the error for the v and w directions are computed similarly. In Table 2a, we report the ℓ_1 norm of the error in uncontrolled reduced order approximations using $\mathcal{N}_R = 3, 6, 9$ and 12 basis functions ($N_R = 1, 2, 3, 4$). The basis functions used here are the same as those employed in Figures 3 and 4. The condition numbers of the resulting mass and stiffness matrices $(K_E^{2\mathcal{N}_R}, M^{2\mathcal{N}_R})$ are tabulated in Table 2b. Note that in these simulations, the reduced basis elements were chosen so that the ℓ_1 error decreases as the span of the reduced basis space increases. The convergence stops at 12 basis functions where it could be seen in Table 2a that the reported best approximation we could obtain with 12 basis functions produced an error the same level as the approximation with 9 basis functions. From Table 2b, condition numbers above 1×10^7 with 12 basis functions suggest that we can expect no further convergence due to poor conditioning. To further illustrate how random snapshots of the state might not be well suited as basis functions in reduced model applications, we present examples in Tables 3a and 3b where basis functions were chosen to give larger errors than in Table 2a.

It must also be noted that simple linear independence is not a sufficient criterion for choosing basis functions since linearly dependent functions that result in condition numbers above 1×10^{10} could result in an unstable system matrix $A^{2\mathcal{N}}$.

Dimensions	Parameters
$h = .00127m$	$\rho = 2700kg/m^3$
$R = .4m$	$E = 7.1 \times 10^{10} N/m^2$
$\ell = 1m$	$c_D = 1.47 \times 10^5 Nms$
	$\nu = .33$

Table 1. Dimensions and physical parameters of the shell.

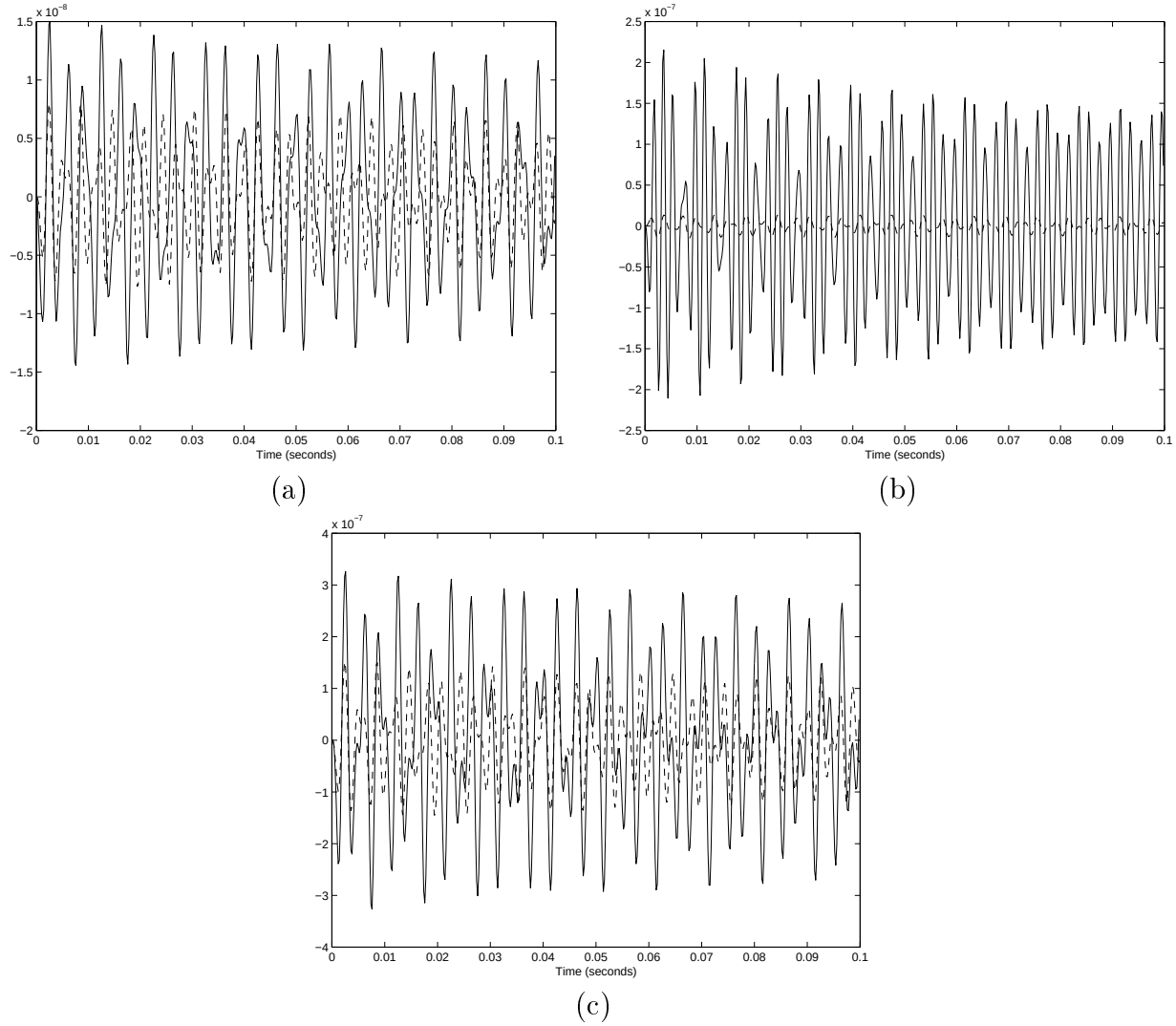

Figure 3. Full order uncontrolled shell displacements at the point p_1 having coordinates $(\hat{x}, \hat{\theta}) = (3\ell/4, \pi/4)$ together with reduced order uncontrolled approximation using $\mathcal{N}_R = 3$ basis functions $(N_R = 1)$; (a) longitudinal $u^{\mathcal{N}}(t, \hat{x}, \hat{\theta})$, (b) circumferential $v^{\mathcal{N}}(t, \hat{x}, \hat{\theta})$, (c) transverse $w^{\mathcal{N}}(t, \hat{x}, \hat{\theta})$; — full order, – – reduced order.

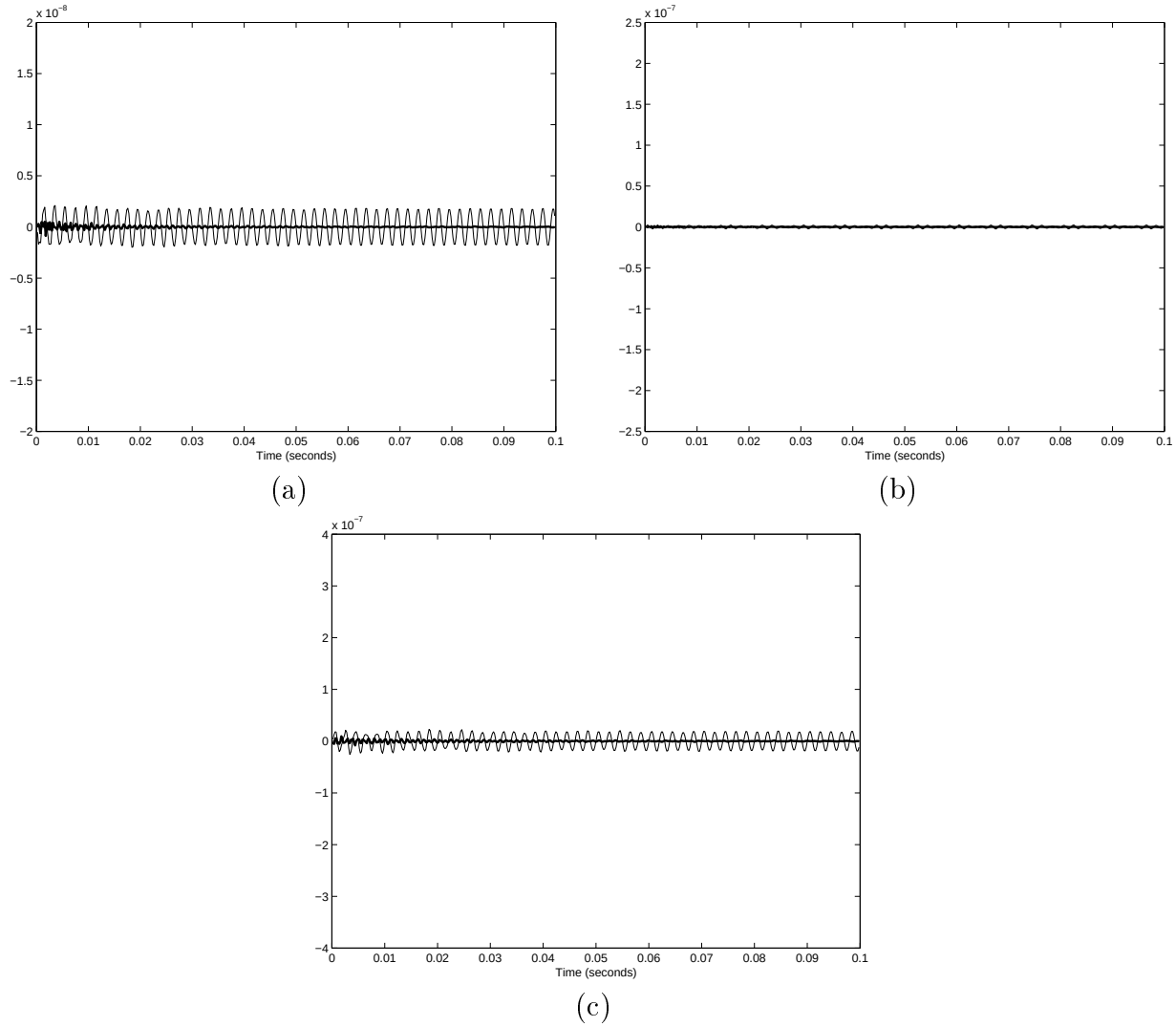

Figure 4. Difference between uncontrolled full and reduced basis shell displacements at the point p_1 having coordinates $(\hat{x}, \hat{\theta}) = (3\ell/4, \pi/4)$; (a) longitudinal $u^{\mathcal{N}}(t, \hat{x}, \hat{\theta})$, (b) circumferential $v^{\mathcal{N}}(t, \hat{x}, \hat{\theta})$, (c) transverse $w^{\mathcal{N}}(t, \hat{x}, \hat{\theta})$; —— $\mathcal{N}_R = 6$ basis functions ($N_R = 2$), —— $\mathcal{N}_R = 9$ basis functions ($N_R = 3$).

$\mathcal{N}_R$	$\|u^{\mathcal{N}} - u^{\mathcal{N}_R}\|_{\ell_1}$	$\|v^{\mathcal{N}} - v^{\mathcal{N}_R}\|_{\ell_1}$	$\|w^{\mathcal{N}} - w^{\mathcal{N}_R}\|_{\ell_1}$	time instance realization t_i
3	2.9275e-06	4.0619e-05	5.8057e-05	.1 s
6	5.7142e-07	5.9078e-07	5.9258e-06	.05, .1 s
9	3.0921e-08	6.4030e-08	5.1482e-07	.033, .067, .1 s
12	3.2560e-08	8.9845e-08	6.1312e-07	$0.002, 0.05, 0.067, 0.1s$

Table 2a. ℓ_1 norm of the difference between full and reduced order models using 3, 6, 9 and 12 basis functions; t_i is the time instance where the reduced basis function $\Upsilon_i(t_i, x, \theta)$ is realized; basis functions were chosen to obtain convergence as the dimension of reduced basis space increases.

$\mathcal{N}_R$	$\kappa(M)$	$\kappa(K_E)$	time instance realization t_i
3	1.13e+00	8.63e+02	$t_i = .1\ s$
6	4.08e+01	1.03e+04	$t_i = .05, .1\ s$
9	4.39e+04	1.46e+05	$t_i = .033, .067, .1\ s$
12	6.43e+07	3.05e+08	$t_i = 0.002, 0.05, 0.067, 0.1s$

Table 2b. Condition numbers of the mass and stiffness matrices (M and K_E) from basis functions formed in Table 2a; t_i is the time instance where the reduced basis function $\Upsilon_i(t_i, x, \theta)$ is realized.

$\mathcal{N}_R$	$\|u^{\mathcal{N}} - u^{\mathcal{N}_R}\|_{\ell_1}$	$\|v^{\mathcal{N}} - v^{\mathcal{N}_R}\|_{\ell_1}$	$\|w^{\mathcal{N}} - w^{\mathcal{N}_R}\|_{\ell_1}$	time instance realization t_i
3	2.9275e-06	4.0619e-05	5.8057e-05	$.1\ s$
6	4.6502e-07	1.0696e-05	7.3875e-06	$.033, .1\ s$
9	5.8223e-08	1.6848e-07	1.1434e-06	$.033, .05, .1\ s$
12	3.0333e-07	1.9144e-07	4.1073e-06	$0.002, 0.05, 0.075, 0.1s$

Table 3a. ℓ_1 norm of the difference between full and reduced order models using 3, 6, 9 and 12 basis functions; t_i is the time instance where the reduced basis function $\Upsilon_i(t_i, x, \theta)$ is realized; for the discretization levels 6, 9 and 12, basis functions were chosen to give larger ℓ_1 norm of the error than in Table 2a.

$\mathcal{N}_R$	$\kappa(M)$	$\kappa(K_E)$	time instance realization t_i
3	1.13e+00	8.63e+02	$t_i = .1\ s$
6	2.16e+00	1.15e+03	$t_i = .033, .1\ s$
9	4.53e+04	4.66e+05	$t_i = .033, .05, .1\ s$
12	3.89e+07	1.12e+09	$t_i = 0.002, 0.05, 0.075, 0.1s$

Table 3b. Condition numbers of the mass and stiffness matrices (M and K_E) from basis functions formed in Table 3a; t_i is the time instance where the reduced basis function $\Upsilon_i(t_i, x, \theta)$ is realized.

4.1.2 LQR Control with Periodic Exogenous Input

In this section, we present results where the feedback law described in [10] and [11] is employed in a reduced basis model for the shell acted upon by the external force – see (14) – given in the previous example. The reduced basis functions are first created using snapshots from the *uncontrolled* full order system. Feedback gains based on Riccati operators $\Pi^{2\mathcal{N}_R}$ and optimal controls $U(t)$ in the $\mathcal{N}_R$ dimensional reduced basis space are determined by minimizing the standard quadratic functional

$$J(u, z_0) = \frac{1}{2}\int_0^\tau \left\{ \left\langle Q^{2\mathcal{N}_R} z^{2\mathcal{N}_R}(t), z^{2\mathcal{N}_R}(t) \right\rangle + \left\langle R^{2s} U(t), U(t) \right\rangle \right\} dt \tag{16a}$$

subject to the system

$$\begin{aligned} \dot{z}^{2\mathcal{N}_R}(t) &= A^{2\mathcal{N}_R} z^{2\mathcal{N}_R}(t) + B^{2\mathcal{N}_R} U(t) + G^{2\mathcal{N}_R}(t) \\ z^{2\mathcal{N}_R}(0) &= z_0^{2\mathcal{N}_R} \ , \end{aligned} \tag{16b}$$

where τ is the period of the exogenous force $G^{2\mathcal{N}_R}$ and $U(t) \in \mathbb{R}^{2s}$ (s is the number of patch pairs). The displacements and voltages to the patches are weighted using the matrices $Q^{2\mathcal{N}_R}$ and R^{2s}, respectively. As detailed in Chapters 8 and 9 of [4], the optimal control which minimizes (16a) is given in feedback form by

$$\overline{U}(t) = -R^{2s} \left(B^{2\mathcal{N}_R}\right)^T \left[\Pi^{2\mathcal{N}_R} \bar{z}^{2\mathcal{N}_R}(t) - r^{2\mathcal{N}_R}(t)\right] \ , \tag{17}$$

where the τ-periodic trajectory $\bar{z}^{2\mathcal{N}_R}(t)$ is obtained by solving the closed loop system

$$\begin{aligned} \dot{z}^{2\mathcal{N}_R}(t) &= \left[A^{2\mathcal{N}_R} - B^{2\mathcal{N}_R} \left(R^{2s}\right)^{-1} (B^{2\mathcal{N}_R})^T \Pi^{2\mathcal{N}_R}\right] z^{2\mathcal{N}_R}(t) \\ &- B^{2\mathcal{N}_R} \left(R^{2s}\right)^{-1} (B^{2\mathcal{N}_R})^T r^{2\mathcal{N}_R}(t) + G^{2\mathcal{N}_R}(t) \\ z^{2\mathcal{N}_R}(0) &= 0 \ . \end{aligned} \tag{18}$$

The Riccati variable $\Pi^{2\mathcal{N}_R}$ and tracking variable $r^{2\mathcal{N}_R}(t)$ satisfy the equations

$$(A^{2\mathcal{N}_R})^T \Pi^{2\mathcal{N}_R} + \Pi^{2\mathcal{N}_R} A^{2\mathcal{N}_R} - \Pi^{2\mathcal{N}_R} B^{2\mathcal{N}_R} \left(R^{2s}\right)^{-1} (B^{2\mathcal{N}_R})^T \Pi^{2\mathcal{N}_R} + Q^{2\mathcal{N}_R} = 0 \ , \tag{19}$$

and

$$\begin{aligned} \dot{r}^{2\mathcal{N}_R}(t) &= -[A^{2\mathcal{N}_R} - B^{2\mathcal{N}_R} \left(R^{2s}\right)^{-1} (B^{2\mathcal{N}_R})^T \Pi^{2\mathcal{N}_R}]^T r^{2\mathcal{N}_R}(t) + \Pi^{2\mathcal{N}_R} G^{2\mathcal{N}_R}(t) \\ r^{2\mathcal{N}_R}(\tau) &= 0 \ , \end{aligned} \tag{20}$$

respectively.

Twelve patch pairs bonded to the shell are used as actuators. The dimensions and material properties for both the shell and patches are given in Table 4. All patches are assumed to have a uniform dimension of x length $= 0.1m$ and θ width $= \pi/6$ with the location of the center of each pair summarized in Table 4.

	Dimensions	Parameters
Shell	$h = .00127m$ $R = .4m$ $\ell = 1m$	$\rho = 2700kg/m^3$ $E = 7.1 \times 10^{10} N/m^2$ $c_D = 1.47 \times 10^5 Nms$ $\nu = .33$
Patches	$h_{pe} = .0001778m$ Centers (x, θ): (.25,0), (.5,0), (.75,0) $(.25, \pi/2)$, $(.5, \pi/2)$, $(.75, \pi/2)$ $(.25, \pi)$, $(.5, \pi)$, $(.75, \pi)$ $(.25, 3\pi/2)$, $(.5, 3\pi/2)$, $(.75, 3\pi/2)$	$\rho_{pe} = 7600kg/m^3$ $E_{pe} = 6.3 \times 10^{10} N/m^2$ $c_{D_{pe}} = 1.7 \times 10^5 Nms$ $\nu_{pe} = .31$ $d_{31} = 190 \times 10^{-12} m/V$

Table 4. Dimensions and physical parameters for the shell and patches.

The matrix $Q^{2\mathcal{N}_R}$ was taken to be

$$Q^{2\mathcal{N}_R} = \begin{bmatrix} d_1 I & & & & \\ & d_2 I & & & \\ & & \ddots & & \\ & & & d_5 I & \\ & & & & d_6 I \end{bmatrix}_{2\mathcal{N}_R \times 2\mathcal{N}_R} \times \begin{bmatrix} K_E^{\mathcal{N}_R} & \\ & M^{\mathcal{N}_R} \end{bmatrix}_{2\mathcal{N}_R \times 2\mathcal{N}_R} , \tag{21}$$

where the identity matrix I is $N_R \times N_R$, and $M^{\mathcal{N}_R}$ and $K_E^{\mathcal{N}_R}$ denote the mass and stiffness matrices. To maximize displacement attenuation, the value $d_i = 1 \times 10^{13}, i = 1, \ldots, 6$ was used, and to limit the voltage input to the patches around 100 volts, the matrix of control weights R^{2s} was taken to be the diagonal matrix $R^{2s} = 50 \cdot I^{2s \times 2s}$. Note that these weights are identical to the values used in full order calculations in [11].

After creating the system matrices, the Riccati equation (19) was numerically solved and the tracking equation (20) was integrated backwards in time, from $t = \tau$ to $t = 0$. The controlled displacements at the point p_1 were obtained by numerically integrating the closed loop (18) from $t = 0$ to $t = 0.1$ and recording point displacements at 500 time instances. In Figure 5, we indicate the location of the point p_1 on the shell together with the location of the lines $L_1 = \{(x, \theta) | 0 \leq x \leq \ell, \theta = \pi/6\}$ and $L_2 = \{(x, \theta) | x = 3\ell/4, 0 \leq \theta \leq 2\pi\}$ where root mean square (RMS) displacements of the uncontrolled and controlled simulations are computed. By taking 500 samples at each point on the RMS lines, the root mean square displacements on L_1 and L_2 in the longitudinal direction are computed using

$$\begin{aligned} L_1^{RMS}(x) &= \sqrt{\frac{1}{500} \sum_{i=0}^{500} u^{\mathcal{N}_R}(t_i, x, \pi/6)^2} \ , \ 0 \leq x \leq \ell \\ L_2^{RMS}(\theta) &= \sqrt{\frac{1}{500} \sum_{i=0}^{500} u^{\mathcal{N}_R}(t_i, 3\ell/4, \theta)^2} \ , \ 0 \leq \theta \leq 2\pi \ . \end{aligned}$$

RMS displacements in the circumferential and transverse directions (v and w) on L_1 and L_2 are calculated similarly. Also depicted in Figure 5 is the spatial distribution of the external force (14) modeled to excite the shell.

In Figure 6a, the plots of the uncontrolled and controlled displacements at the point p_i using 6 reduced basis functions ($N_R = 2$) indicate that we get attenuation levels of approximately 99%. Root mean square displacements of the uncontrolled and controlled displacements showing the same degree of attenuation are plotted in Figure 6b.

As illustrated in the example of Section 4.1.1, $\mathcal{N}_R = 3$ basis functions ($N_R = 1$) were not enough to resolve shell dynamics. In this case we obtained substantial attenuation using the associated feedback control design. However, this is not presented since the reduced order model trajectories did not approximate well the full order model displacements. The reduced order model with $\mathcal{N}_R = 9$ basis functions ($N_R = 3$) demonstrated the same level of attenuation as with $\mathcal{N}_R = 6$ basis functions shown in Figures 6a and 6b. Hence, numerical graphs for $\mathcal{N}_R = 9$ are not given here.

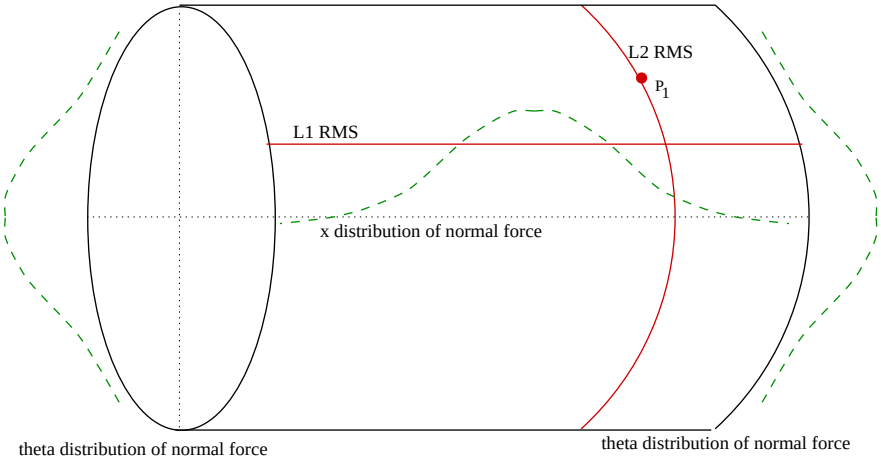

Figure 5. Location of the point p_1, RMS lines $L_1 = \{(x,\theta)|0 \leq x \leq \ell, \theta = \pi/6\}$ and $L_2 = \{(x,\theta)|x = 3\ell/4, 0 \leq \theta \leq 2\pi\}$ and spatial distribution of the exogenous force.

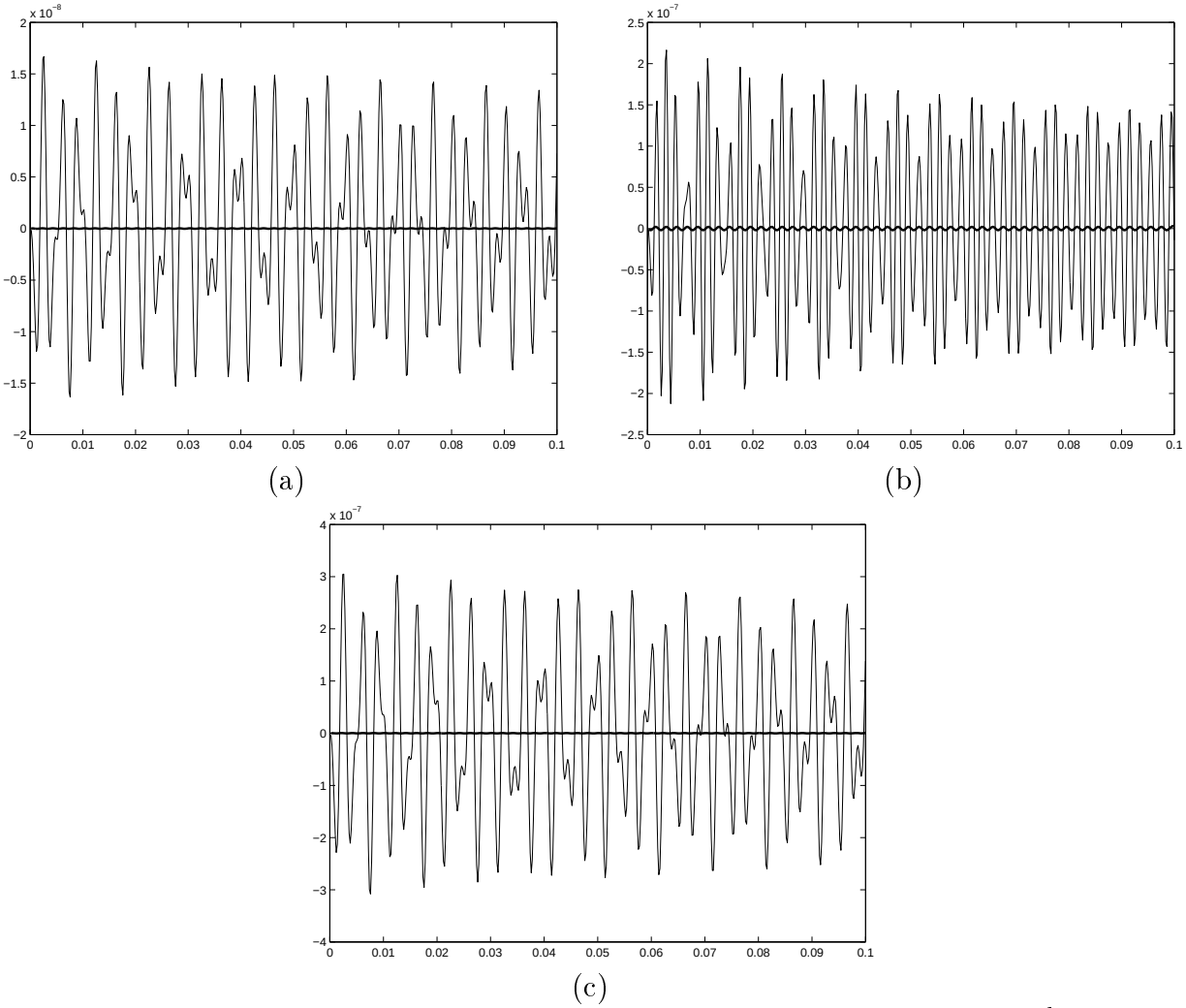

(a) (b) (c)

Figure 6a. Uncontrolled and controlled displacements at the point p_1 with $\mathcal{N}_R = 6$ basis functions ($N_R = 2$); (a) longitudinal $u^{\mathcal{N}_R}(t,\hat{x},\hat{\theta})$, (b) circumferential $v^{\mathcal{N}_R}(t,\hat{x},\hat{\theta})$, (c) transverse $w^{\mathcal{N}_R}(t,\hat{x},\hat{\theta})$; —— (uncontrolled), ▬▬ (controlled).

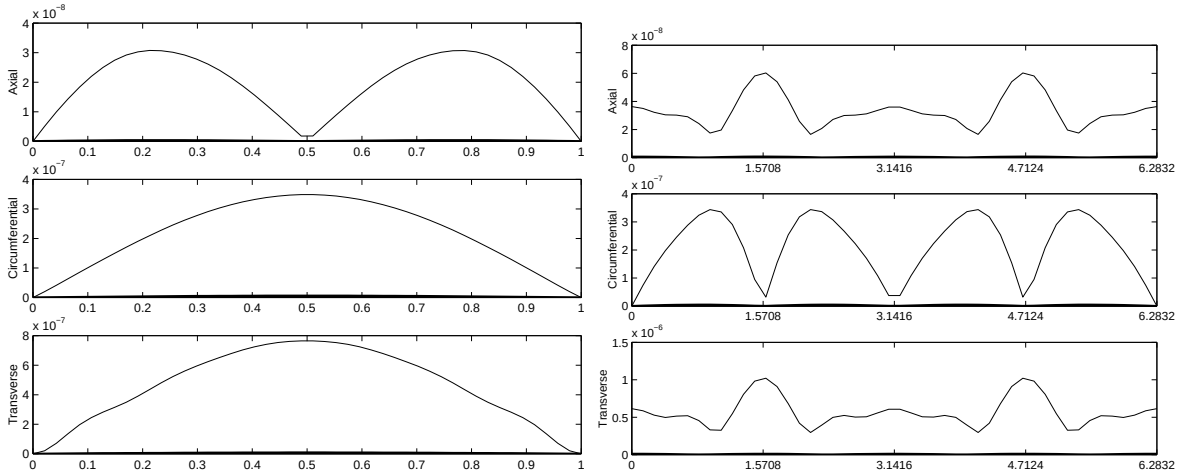

Figure 6b. Root mean square displacements with $\mathcal{N}_R = 6$ basis functions ($N_R = 2$); (a) axial line L_1, (b) circumferential line L_2; —— (uncontrolled), ▬▬ (controlled).

The best attenuation obtained with $\mathcal{N}_R = 12$ basis functions ($N_R = 4$) are presented in Figures 7a and 7b, where displacements and RMS plots are illustrated. As seen from the graphs, the attenuation was not as good as in the case with $\mathcal{N}_R = 6$ or 9 basis functions. Large condition numbers of the mass and stiffness matrices (see Table 2b) suggest that ill-conditioning could have been a factor in numerical difficulty when computing control gains. Aside from condition numbers, the standard control theory notion of *controllability* could also be used to aid in evaluation of the chosen reduced basis elements. It is a necessary (but not sufficient) condition for a linear system to be driven to zero starting at any initial state. Linear systems described by the matrices $A^{2\mathcal{N}_R}$ and $B^{2\mathcal{N}_R}$ in the first order linear system (16b) are *controllable* if the $2\mathcal{N}_R \times 2s\mathcal{N}_R$ controllability matrix $\mathcal{C}(A^{2\mathcal{N}_R}, B^{2\mathcal{N}_R}) = [B|AB|A^2B|\cdots|A^{2\mathcal{N}_R-1}B]$, where $A \equiv A^{2\mathcal{N}_R}, B \equiv B^{2\mathcal{N}_R}$, has rank $2\mathcal{N}_R$. For systems with rank $\left(\mathcal{C}(A^{2\mathcal{N}_R}, B^{2\mathcal{N}_R})\right) = m \leq 2\mathcal{N}_R$, any initial condition of the state $z^{2\mathcal{N}_R}$ in the m dimensional subspace of $\mathbb{R}^{2\mathcal{N}_R}$ spanned by the columns of $\mathcal{C}(A^{2\mathcal{N}_R}, B^{2\mathcal{N}_R})$ can be driven to zero (see [8]). Generally speaking, the larger the deficit of $\mathcal{C}(A^{2\mathcal{N}_R}, B^{2\mathcal{N}_R})$ from its maximum possible rank, the more difficulty in stabilizing or controlling the linear system (16b). A summary of the ranks of the controllability matrix for the different numbers of basis functions is given in Table 5, where it is seen that the ratio of rank to maximum possible rank is constant with $\mathcal{N}_R = 3, 6, 9$ but then drops dramatically with 12 basis functions. Thus, aside from ill-conditioning, the poor rank of the controllability matrix with 12 basis functions suggest a possible explanation to the poor attenuation results reported in Figures 7a and 7b.

We point out again that different scales in the u, v and w directions are used in Figures 6a, 6b, 7a and 7b due to the different orders of magnitudes of the displacements.

Summarizing our experiences, we note that the Lagrange reduced basis method is effective with the correct choice of basis elements but is extremely sensitive to improved accuracy by the addition of more elements in the basis. Appropriate choice of basis elements depends heavily on user intuition. Linear independence is not sufficiently intuitive to use in choosing the basis functions since linearly dependent snapshots could seem to be very different when

plotted, while on the other hand mesh plots of the snapshots could seem identical to the user and yet they might be linearly independent.

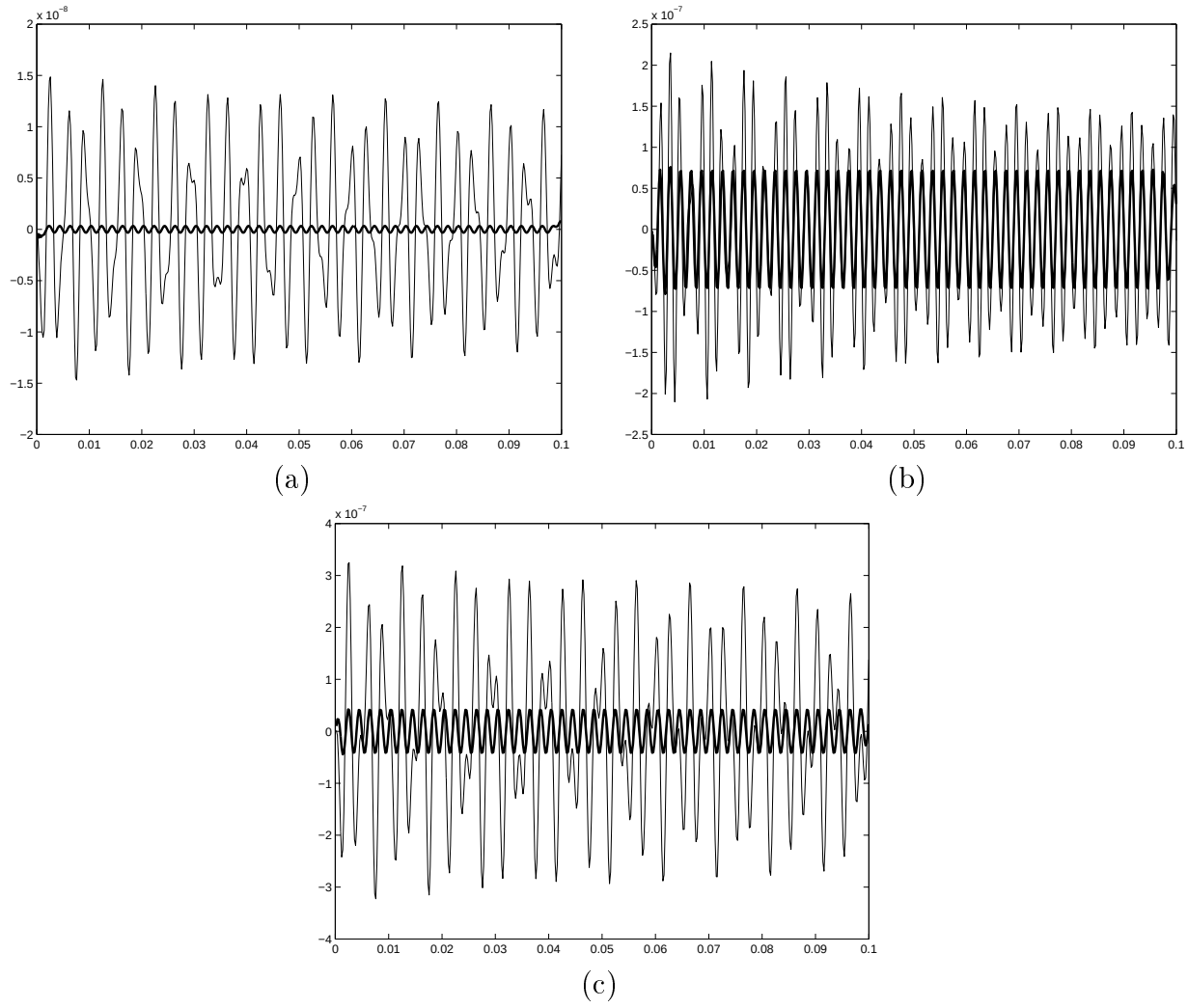

Figure 7a. Uncontrolled and controlled displacements at the point p_1 with $\mathcal{N}_R = 12$ basis functions ($N_R = 4$); (a) longitudinal $u^{\mathcal{N}_R}(t, \hat{x}, \hat{\theta})$, (b) circumferential $v^{\mathcal{N}_R}(t, \hat{x}, \hat{\theta})$, (c) transverse $w^{\mathcal{N}_R}(t, \hat{x}, \hat{\theta})$; —— (uncontrolled), —— (controlled).

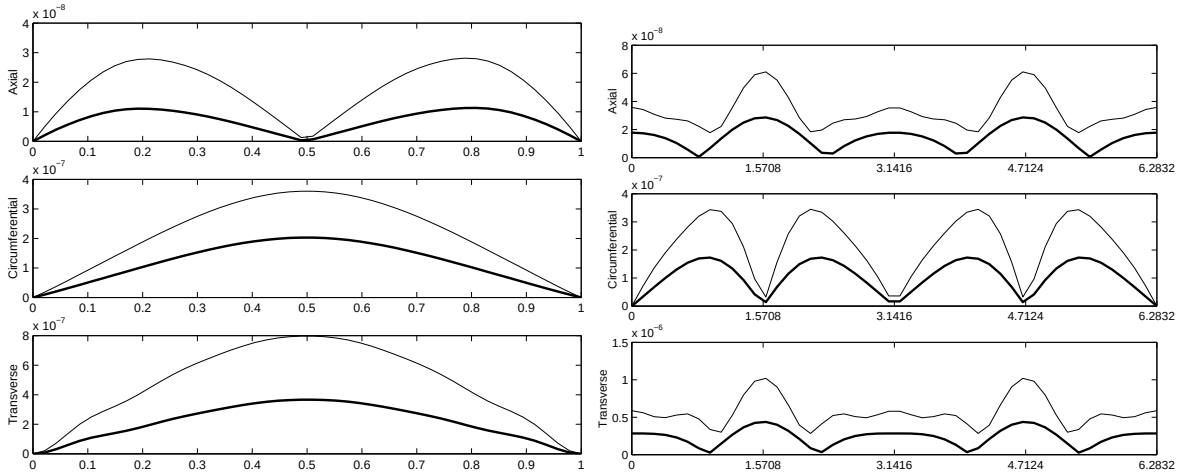

Figure 7b. Root mean square displacements with $\mathcal{N}_R = 12$ basis functions ($N_R = 4$); (a) axial line L_1, (b) circumferential line L_2; —— (uncontrolled), ▬▬ (controlled).

$\mathcal{N}_R$	time instance realization t_i	rank($\mathcal{C}(A^{2\mathcal{N}_R}, B^{2\mathcal{N}_R})$)/max possible rank
3	.1 s	2/6
6	.05, .1 s	4/12
9	.033, .067, .1 s	6/18
12	0.02, 0.05, 0.67, 0.1 s	6/24

Table 5. Rank of the controllability matrix $\mathcal{C}(A^{2\mathcal{N}_R}, B^{2\mathcal{N}_R})$; t_i is the time instance where the reduced basis function $\Upsilon_i(t_i, x, \theta)$ is realized; the ratios in the last column indicate the rank of the controllability matrix over the maximum possible rank. Condition numbers of the mass and stiffness matrices are given in Table 2b.

5 Proper Orthogonal Decomposition (POD)

A possible remedy for some of the difficulties (e.g., growing condition numbers, difficulty in choosing linearly independent elements) encountered with the reduced basis method lies in the use of the proper orthogonal decomposition (POD) method. This alternative method provides a systematic way of creating a reduced basis space using the same information as the Lagrange reduced basis method, i.e., the state of the system at different time instances. As in general reduced order basis methods, the states could come from full order numerical computations or from experimental data.

Given N_s snapshots of the model $\{y_i(x,\theta)\}_{i=1}^{N_s}$ at time instances $t_1, \ldots, t_{N_s}$, we seek basis elements of the form

$$\Phi_j(x,\theta) = \sum_{i=1}^{N_s} \bar{\alpha}_i^j y_i(x,\theta) \ . \tag{22}$$

The POD basis element $\Phi_j(x,\theta)$ is chosen to resemble $\{y_i(x,\theta)\}_{i=1}^{N_s}$ in the sense that it maximizes

$$\frac{1}{N_s}\sum_{i=1}^{N_s}|\langle y_i,\Phi\rangle|^2 \ ,$$

subject to

$$\langle\Phi,\Phi\rangle = \|\Phi\|^2 = 1 \ .$$

As described in [7, 16], the coefficients $\bar{\alpha}^j \in \mathbb{R}^{N_s}$ of (22) are taken to be eigenvectors of the covariant matrix C given by

$$[C]_{k\ell} = \frac{1}{N_s}\langle y_k, y_\ell\rangle \quad , \ k,\ell = 1,\ldots,N_s \ . \tag{23}$$

Since the matrix C is nonnegative and Hermitian, it has a complete set of orthogonal eigenvectors with corresponding eigenvalues $\lambda_1 \geq \lambda_2 \geq \ldots \geq \lambda_{N_s} \geq 0$. We choose the eigenvectors such that

$$\bar{\alpha}^k \cdot \bar{\alpha}^\ell = \begin{cases} 0 \ , & k \neq \ell \\ \dfrac{1}{N_s\lambda_k} \ , & k = \ell \ . \end{cases}$$

The basis elements Φ_j are shown to be orthonormal in [16]. Furthermore, the following lemma from [16] establishes the optimality of the basis $\{\Phi_j\}$ in the sense that the approximation $y^{\mathcal{N}_P}$ using the POD basis to the solution $y \in L^2(0,T;L^2(\Gamma_0))$ contains the most "displacement energy" possible in a time average sense. (For a full discussion of this measure of optimality of the POD method, see for example, [7]).

Lemma 1 *Let $\{\Phi_1,\Phi_2,\ldots,\Phi_{N_s}\}$ denote the orthonormal set of POD basis elements and $\lambda_1 \geq \lambda_2 \geq \ldots \geq \lambda_{N_s}$ denote the corresponding set of eigenvalues. If*

$$y^N(t,x,\theta) = \sum_{i=1}^{N_s} b_i(t)\Phi_i(x,\theta)$$

denotes the approximation to y with respect to this basis, then the following hold:

1. $\left\langle b_i(t)b_j^*(t)\right\rangle = \delta_{ij}\lambda_i$
2. *For every N_s,*

$$\sum_{i=1}^{N_s}\left\langle b_i(t)b_j^*(t)\right\rangle = \sum_{i=1}^{N_s}\lambda_i \geq \sum_{i=1}^{N_s}\left\langle a_i(t)a_j^*(t)\right\rangle \ ,$$

where

$$y^N(t,x,\theta) = \sum_{i=1}^{N_s} a_i(t)\psi_i(x,\theta)$$

is an approximation to y using any arbitrary orthonormal basis $\{\psi_j\}_{j=1}^{N_s}$.

To determine the dimension of the reduced basis space, we find an integer N_P such that the sum of the first N_P eigenvalues gives a good approximation to the sum of all the eigenvalues, i.e., $\sum_{i=1}^{N_P} \lambda_i \simeq \sum_{i=1}^{N_s} \lambda_i$. The ratio $\sum_{i=1}^{N_P} \lambda_i \Big/ \sum_{i=1}^{N_s} \lambda_i$ gives the percentage energy of the full order model contained in the POD reduced order model. Typically, the first few eigenvalues give a good approximation to the sum of all the eigenvalues. In the numerical examples to be presented, 99% of the energy in the given 20 snapshots of the system was captured by two POD basis elements in each of the three directions u, v, w. After choosing the N_P number of POD basis functions, the POD reduced basis elements are denoted by

$$\Phi_j = \sum_{i=1}^{N_P} \bar{\alpha}_i^j y_i \ , \quad j = 1, \ldots, N_P, \ N_P \ll N_s \ .$$

To implement the method in the shell model, we first take N_s snapshots in each of the u, v and w displacements. The number N_s must be large enough to capture the dynamics of the shell. Then three $N_s \times N_s$ covariant matrices C_u, C_v and C_w are created using the snapshots in u, v and w, respectively from which eigenvalues and eigenvectors are computed – see (23). Then N_P POD basis elements are constructed for each direction with a total of $3N_P$ basis functions which we denote by $\mathcal{N}_P$. We point out that the use of uniform N_P number of basis functions in each direction was done for ease of exposition and that the user could potentially use different values of N_P for each displacement u, v and w. Letting Φ_{u_j}, Φ_{v_j} and Φ_{u_j} denote the N_P POD basis elements in the u, v and w directions, respectively, then the POD reduced basis space is given by

$$V^{\mathcal{N}_P} = \text{span}\{\Phi_{u_j}\}_{j=1}^{N_P} \times \text{span}\{\Phi_{v_j}\}_{j=1}^{N_P} \times \text{span}\{\Phi_{w_j}\}_{j=1}^{N_P} \ , \tag{24}$$

with dimension $\mathcal{N}_P = 3N_P$. Note that since each full order snapshot $u_i^{\mathcal{N}}, v_i^{\mathcal{N}}, w_i^{\mathcal{N}}$ is in $V^{\mathcal{N}}$ for $i = 1, \ldots N_s$ and since each POD basis function is in the span of these snapshots, i.e., $\Phi_{u_j} \in \text{span}\left\{u_i^{\mathcal{N}}\right\}_{i=1}^{N_s}$, $\Phi_{v_j} \in \text{span}\left\{v_i^{\mathcal{N}}\right\}_{i=1}^{N_s}$, and $\Phi_{w_j} \in \text{span}\left\{w_i^{\mathcal{N}}\right\}_{i=1}^{N_s}$, then we have

$$V^{\mathcal{N}_P} \subset V^{\mathcal{N}} \subset V \ . \tag{25}$$

In the reduced basis space $V^{\mathcal{N}_P}$ the first order form of the modeling equations becomes

$$\begin{aligned} \dot{z}^{2\mathcal{N}_P}(t) &= A^{2\mathcal{N}_P} z^{2\mathcal{N}_P}(t) + B^{2\mathcal{N}_P} U(t) + G^{2\mathcal{N}_P}(t) \\ z^{2\mathcal{N}_P}(0) &= z_0^{2\mathcal{N}_P} \ , \end{aligned} \tag{26}$$

where $z^{2\mathcal{N}_P}(t) \in \mathbb{R}^{2\mathcal{N}_P}$.

5.1 Numerical Examples

We illustrate some advantages of the POD reduced order method over the Lagrange reduced order method given in Section 4 by applying the POD method to the example given in Section 4.1.2 and demonstrating that the stiffness and mass matrices remain well conditioned as more basis functions are used. It was shown in Section 4.1.1 that care must be exercised when

adding more Lagrange reduced basis functions or else condition numbers increase dramatically, resulting in computational difficulties.

A second example demonstrates that the performance of the feedback controller designed using the POD model is not degraded by the presence of a large number of frequencies in the exogenous disturbance. This is also done to compare the performance of the POD method with the full order discretization example presented in [11, Example 4].

To obtain the snapshots, we use the full order discretization method employed in the previous sections and obtain $N_s = 20$ realizations of the states between $t = 0$ and $t = 0.1s$. The physical dimensions and properties of the shell and patches are identical with those in the example of Section 4.1.2 and are tabulated in Table 4. For the first example given here, the external exogenous force applied on the shell is given by (14) and (15). In the second example, the x and θ components of the external force also come from (14) and (15) while the temporal components contain five frequencies: 320 Hz, 440 Hz, 600 Hz, 660 Hz and 820 Hz . To model these frequencies, the expression $\sin(1000\pi t)$ in (14) is replaced by

$$g(t) = \sin(640\pi t) + \sin(880\pi t) + \sin(1200\pi t) + \sin(1320\pi t) + \sin(1640\pi t) \ . \tag{27}$$

As in previous numerical examples, point displacements are taken at p_1 while RMS displacements are taken at L_1 and L_2 (see Figure 5).

5.1.1 LQR Control with Periodic Exogenous Input

In Table 2 of Section 4, we indicated that the open loop approximations of the reduced order model exhibited convergence to the full order model (as the dimension of the approximating subspace increased) only if the basis functions were carefully chosen. In some cases, the system matrix $A^{2\mathcal{N}_R}$ of the first order system (11) becomes unstable. Numerical results in this section indicate that those problems can be alleviated somewhat by use of the POD method.

In Table 6 we reveal that the ℓ_1 norm of the difference between solutions of the full and POD reduced order models decreases as the dimension of the reduced basis space increases, with 9 basis functions again appearing to be the upper limit, beyond which further improvement in approximation is difficult to obtain. This behavior is also exhibited by the Lagrange reduced order model as reported in Table 2a. Furthermore, condition numbers of the mass and stiffness matrices remain manageable as more basis functions are added. We point out that even though the ℓ_1 error of the difference between full order and ROM open loop approximations are slightly better in the case of the Lagrange method reported in Table 2a, the basis functions there were chosen, using intuition and trial and error, to give good approximations, and so that level of accuracy is generally much more difficult for users to attain.

The percentage of the full order model energy captured by the POD reduced order model are summarized in Table 7. Note that only $\mathcal{N}_P = 6$ POD basis functions (i.e., $N_P = 2$ basis functions in each direction) were needed to capture 99.99% of the displacement energy of the full order model.

Control authority is maintained as shown in the time history plots in Figure 8. The full order uncontrolled and reduced order controlled displacements of the point p_1 are plotted for the three displacements u, v and w with $\mathcal{N}_R = 6$ basis functions ($N_P = 2$). It is important to note that these calculations compare the full order model uncontrolled displacements (which are indistinguishable from the POD reduced order model uncontrolled displacements) with

those of the POD reduced order model with optimal feedback controller. As expected, the attenuation obtained with $\mathcal{N}_P = 6$ POD basis functions is comparable with the control result with $\mathcal{N}_R = 6$ ROM basis functions (see Figure 6a). Numerical results with $\mathcal{N}_P = 9$ and 12 basis functions ($N_P = 3, 4$) are similar to the results in Figure 8 hence are not presented here.

The full order energy captured by the POD model with $\mathcal{N}_P = 3$ basis functions was only around 60% and it increased to 99.99% with $\mathcal{N}_R = 6$. This behavior of the model is confirmed in Table 6 where the open loop error between the full order and POD reduced order model with $\mathcal{N}_P = 3$ was 2 orders of magnitude larger than with $\mathcal{N}_P = 6$. This suggests that feedback control with 3 POD functions may not be adequate for some practical applications, whereas control design using 6 or 9 POD elements might be.

$\mathcal{N}_P$	$\|u^{\mathcal{N}} - u^{\mathcal{N}_P}\|_{\ell_1}$	$\|v^{\mathcal{N}} - v^{\mathcal{N}_P}\|_{\ell_1}$	$\|w^{\mathcal{N}} - w^{\mathcal{N}_P}\|_{\ell_1}$	$\kappa(M)$	$\kappa(K_E)$
3	1.9905e-05	1.2063e-04	3.8485e-04	1.00	3.08e+02
6	5.5385e-07	5.9334e-07	6.0071e-06	1.00	1.01e+03
9	5.1856e-07	1.6233e-07	2.2242e-06	1.00	1.06e+03
12	4.7084e-07	2.6939e-07	4.3546e-06	1.00	1.96e+03

Table 6. ℓ_1 norm of the difference between uncontrolled full order and uncontrolled POD reduced order models, and condition numbers of the mass matrix (M) and stiffness matrix (K_E) with $\mathcal{N}_P = 3, 6, 9$ and 12 POD basis functions ($N_P = 1, 2, 3$ and 4).

$\mathcal{N}_P$	% u	% v	% w
3	65.059642	58.437199	67.907097
6	99.998964	99.999540	99.99836
9	99.999841	99.999879	99.999501
12	99.999989	99.999998	99.999937

Table 7. Percentage of the full order model energy captured by the POD reduced basis model with $\mathcal{N}_P = 3, 6, 9$ and 12 POD basis functions ($N_P = 1, 2, 3$ and 4).

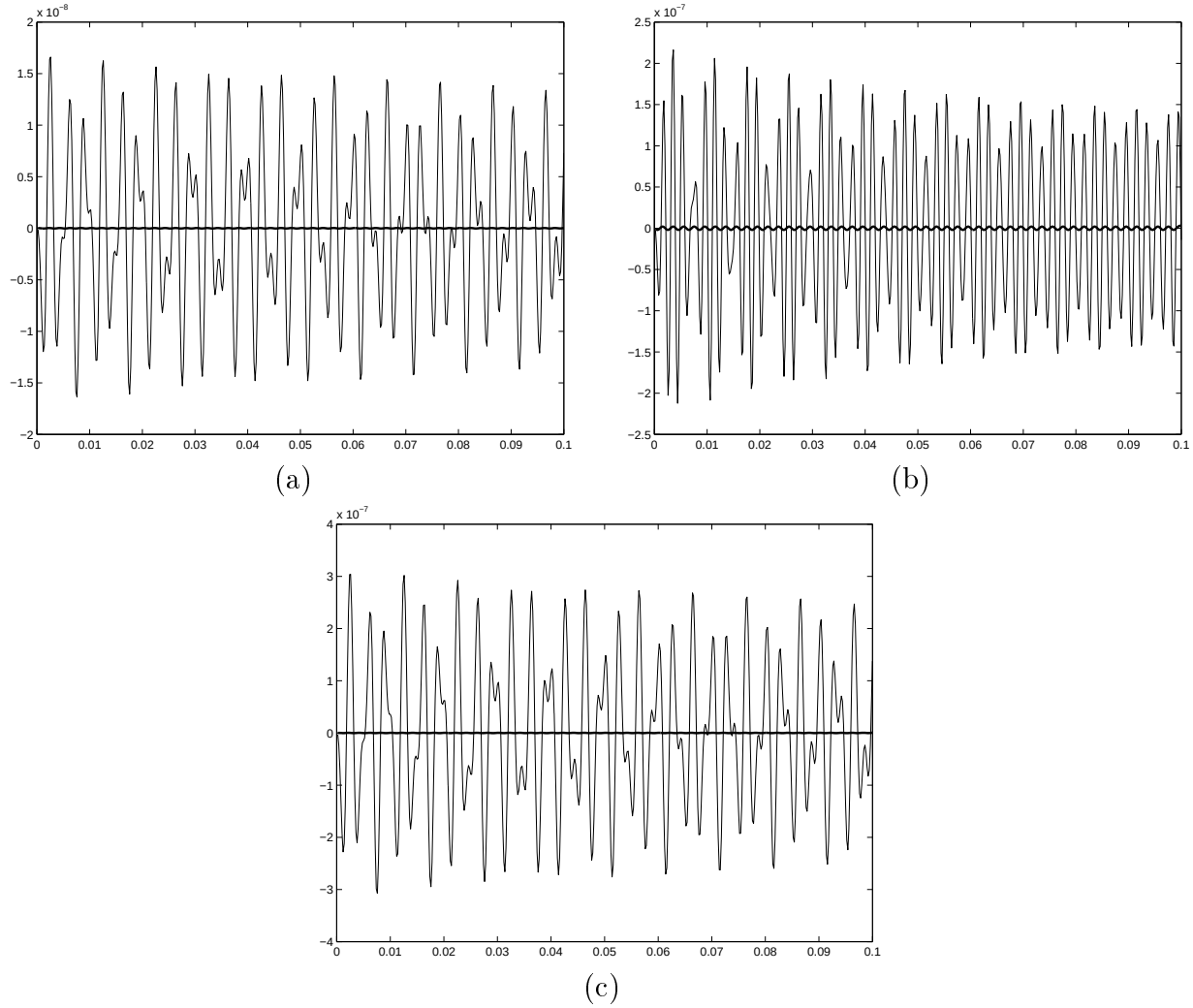

Figure 8. Uncontrolled and controlled displacements at the point p_1 with $\mathcal{N}_P = 6$ POD basis functions; (a) longitudinal $u^{\mathcal{N}_P}(t, \hat{x}, \hat{\theta})$, (b) circumferential $v^{\mathcal{N}_P}(t, \hat{x}, \hat{\theta})$, (c) transverse $w^{\mathcal{N}_P}(t, \hat{x}, \hat{\theta})$; —— (uncontrolled), ▬▬ (controlled).

5.1.2 LQR Control with Multiple Frequency Exogenous Input

In this example, we illustrate that the performance of the controller is not degraded by a larger number of frequencies in the exogenous disturbance by employing an external forcing function whose temporal component is given by (27). Again, the values of the dimension of the POD reduced basis space used in the simulations were $\mathcal{N}_P = 3, 6, 9$ and 12 ($N_P = 1, 2, 3$ and 4). The percentages of the energy captured by the reduced order model are tabulated in Table 8 where it can be seen that the POD model captured less energy (than with a single frequency excitation simulation – see Table 7) of the full order model. As with the single frequency excitation case in the previous example, $\mathcal{N}_P = 3$ basis functions were *not* enough to capture acceptable levels of the full order displacement energy. Displacements of the uncontrolled full order and POD reduced order model with 3 basis functions illustrating that the system is not fully approximated, are plotted in Figure 9.

$\mathcal{N}_P$	% u	% v	% w
3	52.092083	59.426622	54.909536
6	99.895918	99.985078	99.925809
9	99.994818	99.999375	99.993714
12	99.999986	99.999998	99.999773

Table 8. Percentage of the full order model energy captured by the POD reduced basis model.

The uncontrolled and controlled displacements with $\mathcal{N}_P = 6, 9$ and 12 basis functions ($N_P = 2, 3, 4$) exhibited similar dynamics and control attenuation hence only results with $\mathcal{N}_P = 6$ are reported. Displacement plots at the point p_1 are illustrated in Figure 10 while RMS plots are given in Figure 11.

This example with multiple exogenous frequency suggests some robustness of the method with respect to the number of required POD basis functions. More basis functions (than with a single frequency excitation model) are needed to capture the total energy of the full order system due to the larger number of exciting frequencies. Numerical results showing good attenuation using $\mathcal{N}_P = 6, 9$ and 12 basis functions with well conditioned mass and stiffness matrices (reported in Table 9) indicate that computations are not overly sensitive to the increasing number of POD basis functions once convergence is reached. To further illustrate the features of the method, the ranks of the controllability matrix $\mathcal{C}(A^{2\mathcal{N}_P}, B^{2\mathcal{N}_P})$ for each discretization size are given in Table 9. In the last column of the table, the ratios indicate ranks of the controllability and observability matrices over the maximum possible rank of the matrices (which is discussed in controllability contexts). The difficulty in controlling with $\mathcal{N}_R = 12$ Lagrange reduced basis functions, illustrated in Figures 7a and 7b, are not present in the POD reduced order model. Condition numbers (instead of controllability issues) could be a possible explanation for the poor attenuation in the Lagrange model (with $\mathcal{N}_R = 12$) since a comparison of Table 5 and Table 9 indicate that the rank of the controllability matrix $\mathcal{C}(A^{2\mathcal{N}_R}, B^{2\mathcal{N}_R})$ is the same for both cases while the condition number of the stiffness matrix $K_E^{2\mathcal{N}_R}$ in the Lagrange method is 5 magnitudes larger. Moreover, the condition number of the mass matrix in the Lagrange model is 7 orders of magnitude larger.

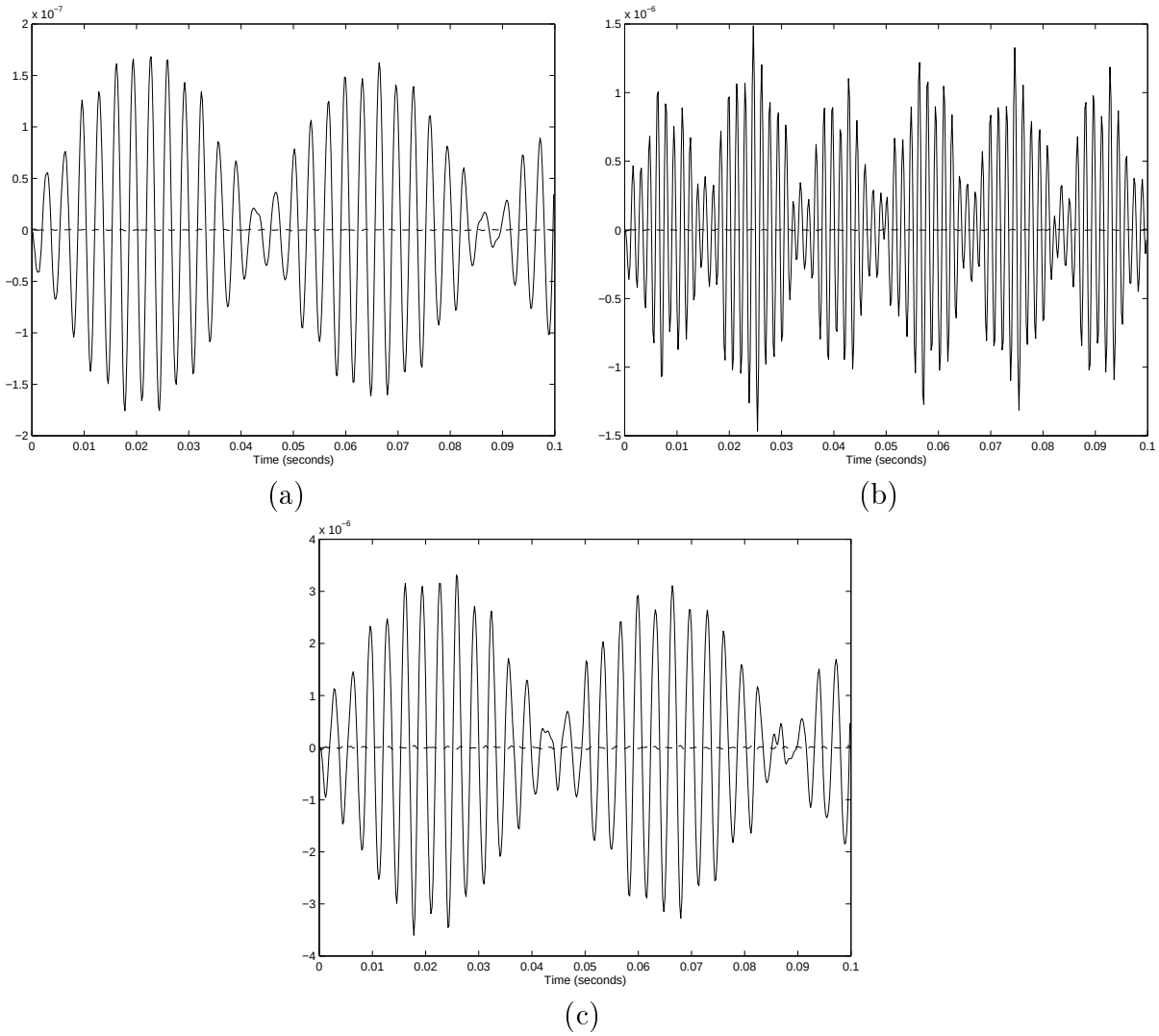

Figure 9. Full and POD reduced order uncontrolled shell displacements at the point p_1 with $\mathcal{N}_P = 3$ POD basis functions ($N_P = 1$); (a) longitudinal $u^{\mathcal{N}}(t, \hat{x}, \hat{\theta})$, (b) circumferential $v^{\mathcal{N}}(t, \hat{x}, \hat{\theta})$, (c) transverse $w^{\mathcal{N}}(t, \hat{x}, \hat{\theta})$; — full order, – – reduced order.

$\mathcal{N}_P$	$\kappa(M)$	$\kappa(K_E)$	rank($\mathcal{C}(A^{2\mathcal{N}_R}, B^{2\mathcal{N}_R})$)/max possible rank
3	1.00	1.15e+01	4/6
6	1.00	1.01e+03	4/12
9	1.00	1.12e+03	6/18
12	1.00	1.93e+03	6/24

Table 9. Condition numbers of the mass matrix M, stiffness matrix K_E and ranks of the controllability matrix $\mathcal{C}(A^{2\mathcal{N}_R}, B^{2\mathcal{N}_R})$. The ratios in the last two columns indicate the actual rank over the maximum possible rank of the matrices.

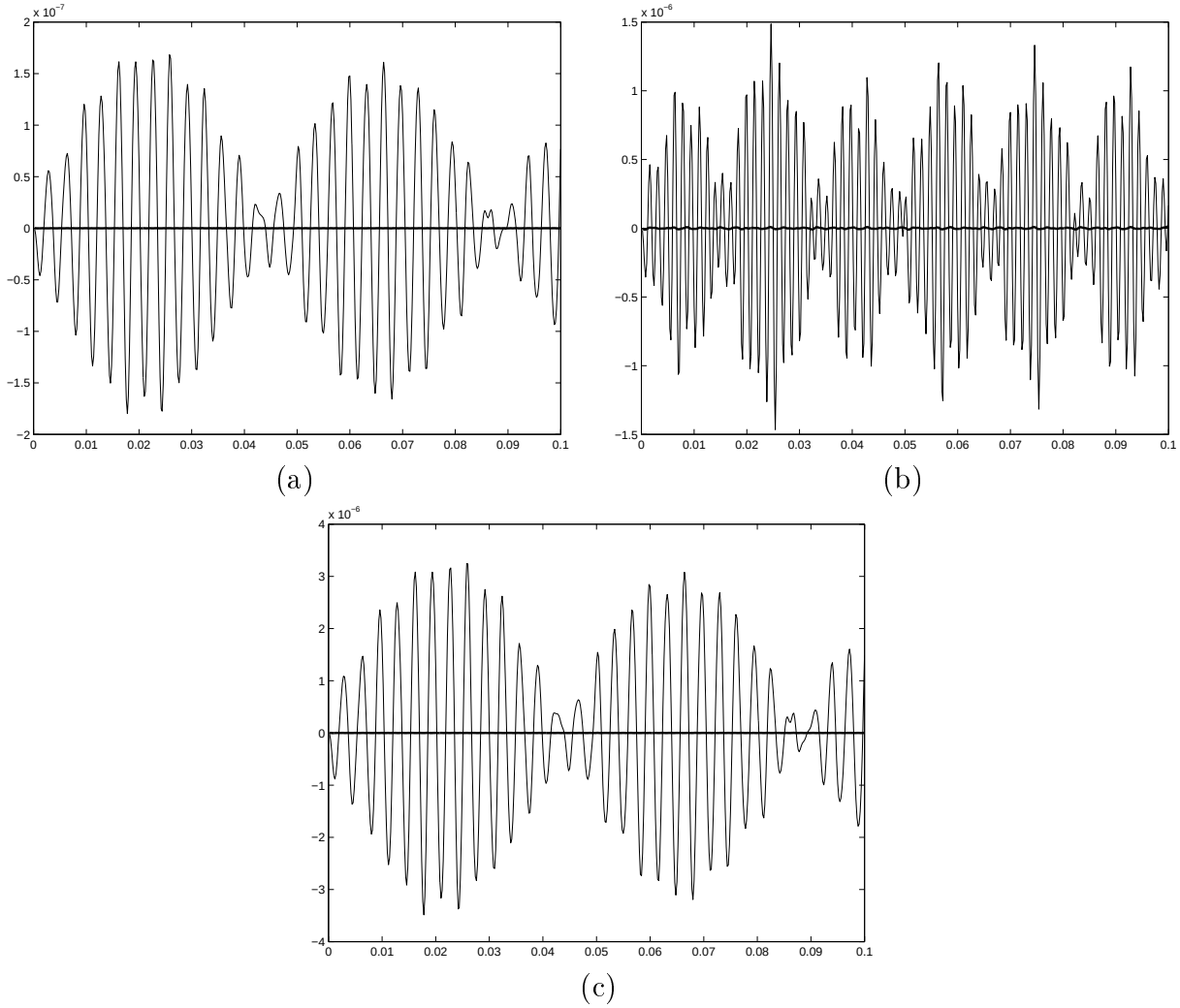

Figure 10. Uncontrolled and controlled displacements at the point p_1 with $\mathcal{N}_P = 6$ POD basis functions ($N_P = 2$); (a) longitudinal $u^{\mathcal{N}_P}(t, \hat{x}, \hat{\theta})$, (b) circumferential $v^{\mathcal{N}_P}(t, \hat{x}, \hat{\theta})$, (c) transverse $w^{\mathcal{N}_P}(t, \hat{x}, \hat{\theta})$; —— (uncontrolled), ▬▬ (controlled).

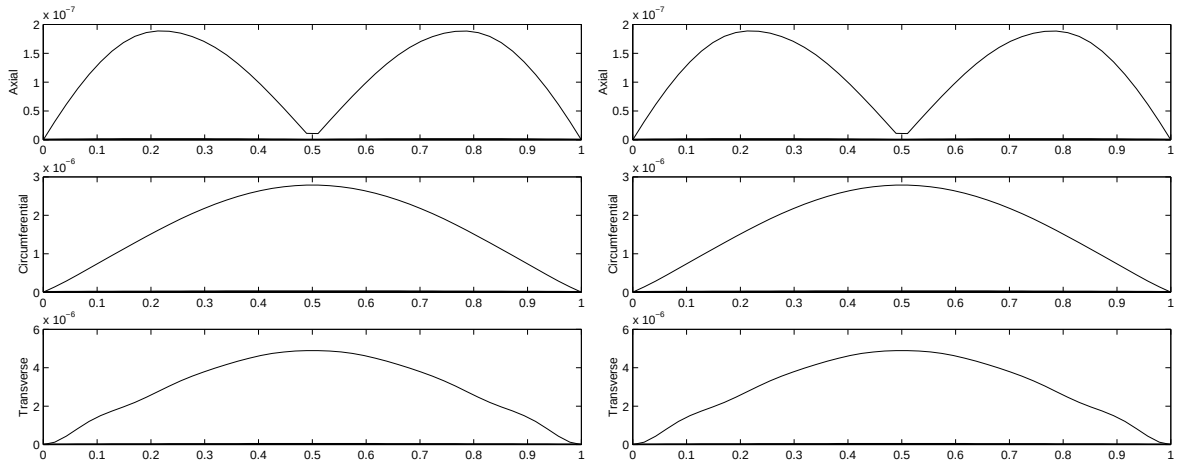

Figure 11. Root mean square displacements with $\mathcal{N}_P = 6$ ($N_P = 2$) POD basis functions; (a) axial line L_1, (b) circumferential line L_2; —— (uncontrolled), ▬▬ (controlled)

6 Reduced order gains applied on the full order system

One primary goal of this research is to be able to compute control gains in real time from observations on a physical shell system using a discretized PDE model and be able to apply the computed control gains in the physical system. Numerical results from model reduction techniques given in previous chapters indicate the possibility of real time computation by reducing the number of unknowns without degrading the performance of the model and without losing control authority. While studies of the ROM designed controllers applied to the ROM dynamics are useful, they are not truly indicative of the performance of the controller when applied in practice. To obtain information in this regard, we next investigated the performance of the reduced order model computed control gains when applied to the physical system. We do this by applying control gains from the reduced order model to the full order model. It has been shown through careful analysis of natural frequencies and modes in [9] that the full order system closely approximates the infinite dimensional system. With the assumption that the full order model closely approximates the infinite dimensional physical system, applying the reduced order gains to the full order system is a reasonable way to investigate the anticipated performance of the method when used on an actual physical system. While our early calculations give *some* indication of how a feedback gain based on reduced order models might perform when applied to either the true infinite dimensional system or even a large finite dimensional model, the results are only suggestive. Further evidence will be available once reduced order model based controllers are implemented experimentally.

In this section, we illustrate the use of reduced order POD gains in controlling the full order system. Although the POD reduced order model is used in the exposition, the method we present could be readily adapted for any type of reduced basis method.

To use the POD reduced order optimal control

$$U(t) = -\left(R^{2s}\right)^{-1}\left(B^{2\mathcal{N}_P}\right)^T\left[\Pi^{2\mathcal{N}_P} z^{2\mathcal{N}_P}(t) - r^{2\mathcal{N}_P}(t)\right] \tag{28}$$

in the full order equation

$$\dot{z}^{2\mathcal{N}}(t) \;=\; A^{2\mathcal{N}} z^{2\mathcal{N}}(t) + B^{2\mathcal{N}} U(t) + G^{2\mathcal{N}}(t)\;, \tag{29}$$

the full order vector of coefficients $z^{2\mathcal{N}}$ must be projected into the expression (28) and substituted with $z^{2\mathcal{N}_P}$. This is necessary to obtain a full order control feedback loop when the reduced order control (28) is employed in (29). Hence we need to find a map $\hat{P} : \mathbb{R}^{2\mathcal{N}} \to \mathbb{R}^{2\mathcal{N}_P}$ mapping $z^{2\mathcal{N}}$ into $z^{2\mathcal{N}_P}$ in order to rewrite (28) as

$$U(t) = -\left(R^{2s}\right)^{-1}\left(B^{2\mathcal{N}_P}\right)^T\left[\Pi^{2\mathcal{N}_P}\hat{P}z^{2\mathcal{N}}(t) - r^{2\mathcal{N}_P}(t)\right]\;. \tag{30}$$

To this end, note first that the Galerkin approximation $y^{\mathcal{N}}$ (of the solution to (5)) is the projection of the infinite dimensional solution y into the finite dimensional subspace $V^{\mathcal{N}}$. Similarly, it follows that $y^{\mathcal{N}_P}$ is the projection of y into $V^{\mathcal{N}_P}$. Denote the projection operator from V into $V^{\mathcal{N}_P}$ by $\mathcal{P}^{\mathcal{N}_P}$ and denote the projection from $V^{\mathcal{N}}$ into $V^{\mathcal{N}_P}$ by $\mathcal{P}^{\mathcal{N}_P}_{V^{\mathcal{N}}}$. The same inner products are used in $V, V^{\mathcal{N}}$ and $V^{\mathcal{N}_P}$ and from (25) we have the space inclusions $V^{\mathcal{N}_P} \subset V^{\mathcal{N}} \subset V$ from which the relationship

$$\mathcal{P}^{\mathcal{N}_P} y^{\mathcal{N}} = \mathcal{P}^{\mathcal{N}_P}_{V^{\mathcal{N}}} y^{\mathcal{N}} = y^{\mathcal{N}_P} \quad \text{for all } y^{\mathcal{N}} \in V^{\mathcal{N}}$$

readily follows. This implies that the reduced order state $(y^{\mathcal{N}_P}, \dot{y}^{\mathcal{N}_P}) \in V^{\mathcal{N}_P} \times V^{\mathcal{N}_P}$ is the projection of the full order state $(y^{\mathcal{N}}, \dot{y}^{\mathcal{N}}) \in V^{\mathcal{N}} \times V^{\mathcal{N}}$ from $V^{\mathcal{N}} \times V^{\mathcal{N}}$ into $V^{\mathcal{N}_P} \times V^{\mathcal{N}_P}$, which is equivalent to mapping the vector of basis coefficients $z^{2\mathcal{N}}$ into $z^{2\mathcal{N}_P}$ (the product spaces arise from the first-order reformulation of the system). We obtain this by pre-multiplying $z^{2\mathcal{N}}$ by the matrix representation of the projection $\mathcal{P}^{\mathcal{N}_P}_{V^{\mathcal{N}}} \times \mathcal{P}^{\mathcal{N}_P}_{V^{\mathcal{N}}}$ from $V^{\mathcal{N}} \times V^{\mathcal{N}}$ into $V^{\mathcal{N}_P} \times V^{\mathcal{N}_P}$. Denoting the matrix representation of $\mathcal{P}^{\mathcal{N}_P}_{V^{\mathcal{N}}}$ by $\bar{P}^{\mathcal{N}_P}$, then $\hat{P}$ which we use in (30) is then given by

$$\hat{P} = \begin{bmatrix} \bar{P}^{\mathcal{N}_P} & \\ & \bar{P}^{\mathcal{N}_P} \end{bmatrix}\;. \tag{31}$$

Note that $\hat{P}$ is the matrix representation of $\mathcal{P}^{\mathcal{N}_P}_{V^{\mathcal{N}}} \times \mathcal{P}^{\mathcal{N}_P}_{V^{\mathcal{N}}}$. The reduced order gains applied on the full order feedback loop, i.e., (30) employed in (29), yields

$$\begin{aligned} \dot{z}^{2\mathcal{N}}(t) \;=\; & \left[A^{2\mathcal{N}} - B^{2\mathcal{N}} R^{-1}\left(B^{2\mathcal{N}_P}\right)^T \Pi^{2\mathcal{N}_P}\hat{P}\right] z^{2\mathcal{N}}(t) \\ & + B^{2\mathcal{N}} R^{-1}\left(B^{2\mathcal{N}_P}\right)^T r^{2\mathcal{N}_P}(t) + G^{2\mathcal{N}}(t)\;. \end{aligned} \tag{32}$$

The computation and structure of the matrix $\bar{P}^{\mathcal{N}_P} \in \mathbb{R}^{\mathcal{N}_P \times \mathcal{N}}$ is dictated by the three component nature of the state $y = (u, v, w)$. The spaces $V^{\mathcal{N}}$ and $V^{\mathcal{N}_P}$ are product spaces as expressed in (8) and (24), respectively; hence the projection $\mathcal{P}^{\mathcal{N}_P}_{V^{\mathcal{N}}}$ would have three components:

$$\begin{aligned} \mathcal{P}^{N_P^u} \;&:\; \text{span}\left\{\mathcal{B}_{u_i}\right\}_{i=1}^{\mathcal{N}_u} \to \text{span}\left\{\Phi_{u_i}\right\}_{i=1}^{N_P} \\ \mathcal{P}^{N_P^v} \;&:\; \text{span}\left\{\mathcal{B}_{v_i}\right\}_{i=1}^{\mathcal{N}_v} \to \text{span}\left\{\Phi_{v_i}\right\}_{i=1}^{N_P} \\ \mathcal{P}^{N_P^w} \;&:\; \text{span}\left\{\mathcal{B}_{w_i}\right\}_{i=1}^{\mathcal{N}_w} \to \text{span}\left\{\Phi_{w_i}\right\}_{i=1}^{N_P}\;. \end{aligned}$$

Denoting the matrix representation of these component projections by $\bar{P}^{N_P^u}$, $\bar{P}^{N_P^v}$ and $\bar{P}^{N_P^w}$, the matrix $\bar{P}^{\mathcal{N}_P}$ has the components

$$\bar{P}^{\mathcal{N}_P} = \begin{bmatrix} \bar{P}^{N_P^u} & & \\ & \bar{P}^{N_P^v} & \\ & & \bar{P}^{N_P^w} \end{bmatrix} .$$

We illustrate the derivation of $\bar{P}^{N_P^u}$ and point out that the derivation of the component matrices $\bar{P}^{N_P^v}$ and $\bar{P}^{N_P^w}$ are carried out similarly. Using the definition of the projection, for $i = 1, \ldots, N_P$ and any $u^{\mathcal{N}} \in \text{span}\,\{\mathcal{B}_{u_i}\}_{i=1}^{\mathcal{N}_u}$, we have

$$\begin{aligned} \left\langle \mathcal{P}^{N_P^u} u^{\mathcal{N}} - u^{\mathcal{N}}, \Phi_{u_i} \right\rangle = 0 \quad &\Rightarrow \quad \left\langle \mathcal{P}^{N_P^u} u^{\mathcal{N}} - \sum_{j=1}^{\mathcal{N}_u} u_j \mathcal{B}_{u_j}, \Phi_{u_i} \right\rangle = 0 \\ &\Rightarrow \quad \left\langle \sum_{k=1}^{N_P} (\bar{P}^{N_P^u} \bar{u})_k \Phi_{u_k} - \sum_{j=1}^{\mathcal{N}_u} u_j \mathcal{B}_{u_j}, \Phi_{u_i} \right\rangle = 0 \ , \end{aligned}$$

where $\bar{u}$ is the vector of coefficients $u_1, \ldots, u_{\mathcal{N}_u}$ in the full order space. The equality $\mathcal{P}^{N_P^u} u^{\mathcal{N}} = \sum_{k=1}^{N_P} (\bar{P}^{N_P^u} \bar{u})_k \Phi_{u_k}$ used above expresses the property of matrix representations where the basis coefficients of the image (i.e., the basis coefficients of $\mathcal{P}^{N_P^u} u^{\mathcal{N}}$ in span $\{\Phi_{u_i}\}_{i=1}^{N_P}$) are obtained by multiplying the matrix representation and the vector of basis coefficients in the domain (i.e., $\bar{P}^{N_P^u} \bar{u}$). We use linear properties of the inner product to obtain

$$\sum_{k=1}^{N_P} (\bar{P}^{N_P^u} \bar{u})_k \left\langle \Phi_{u_k}, \Phi_{u_i} \right\rangle = \sum_{j=1}^{\mathcal{N}_u} u_j \left\langle \mathcal{B}_{u_j}, \Phi_{u_i} \right\rangle \ .$$

Since the equation above is true for $i = 1, \ldots, N_P$, we then form a matrix equation

$$M_1^{N_P \times N_P} (\bar{P}^{N_P^u} \bar{u}) = M_2^{N_P \times \mathcal{N}_u} \bar{u} \ ,$$

where

$$M_1 = \begin{bmatrix} < \Phi_{u_1}, \Phi_{u_1} > & \cdots & < \Phi_{u_{N_P}}, \Phi_{u_1} > \\ \vdots & \ddots & \vdots \\ < \Phi_{u_1}, \Phi_{u_{N_P}} > & \cdots & < \Phi_{u_{N_P}}, \Phi_{u_{N_P}} > \end{bmatrix} \in R^{N_P \times N_P}$$

$$M_2 = \begin{bmatrix} < \mathcal{B}_{u_1}, \Phi_{u_1} > & \cdots & < \mathcal{B}_{u_{\mathcal{N}_u}}, \Phi u_1 > \\ \vdots & \ddots & \vdots \\ < \mathcal{B}_{u_1}, \Phi_{u_{N_P}} > & \cdots & < \mathcal{B}_{u_{\mathcal{N}_u}}, \Phi_{u_{N_P}} > \end{bmatrix} \in R^{N_P \times \mathcal{N}_u} \ .$$

Therefore $\bar{P}^{N_P{}^u} = M_1^{-1} M_2 \in \mathbb{R}^{N_P \times \mathcal{N}_u}$. The other two matrix representations $\bar{P}^{N_P{}^v} \in \mathbb{R}^{N_P \times \mathcal{N}_v}$ and $\bar{P}^{N_P{}^w} \in \mathbb{R}^{N_P \times \mathcal{N}_w}$ are created similarly. Once these matrices are created, the matrix $\hat{P} \in \mathbb{R}^{2\mathcal{N}_P \times 2\mathcal{N}}$ is formed.

In summary, we enumerate the steps taken to implement reduced order gains on the full order model:

1. Create the full order matrices $A^{2\mathcal{N}\times 2\mathcal{N}}, B^{2\mathcal{N}\times 2s}, G^{2\mathcal{N}}$.

2. Run uncontrolled simulation

$$\dot{z}^{2\mathcal{N}}(t) = A^{2\mathcal{N}\times 2\mathcal{N}} z^{2\mathcal{N}}(t) + G^{2\mathcal{N}}(t)$$

   and realize at time steps $t_1, t_2, \ldots, t_{N_s}$.

3. Create covariant matrices C_u, C_v and C_w; obtain eigenvalues and eigenvectors to create the $\mathcal{N}_P = 3N_P$ dimensional POD reduced basis space.

4. Create reduced order matrices $A^{2\mathcal{N}_P\times 2\mathcal{N}_P}, B^{2\mathcal{N}_P\times 2s}, G^{2\mathcal{N}_P}, R^{2s\times 2s}$ and $Q^{2\mathcal{N}_P\times 2\mathcal{N}_P}$ and create the projection matrix $\hat{P} = \hat{P}^{2\mathcal{N}_P\times 2\mathcal{N}}$.

5. Solve the reduced order Riccati equation to obtain the Riccati matrix $\Pi^{2\mathcal{N}_P\times 2\mathcal{N}_P}$.

6. Integrate the reduced order tracking equation

$$\begin{aligned}\dot{r}^{2\mathcal{N}_P}(t) &= -\left[A^{2\mathcal{N}_P\times 2\mathcal{N}_P} - B^{2\mathcal{N}_P\times 2s}\left(R^{2s\times 2s}\right)^{-1}\left(B^{2\mathcal{N}_P\times 2s}\right)^T \Pi^{2\mathcal{N}_P\times 2\mathcal{N}_P}\right] r^{2\mathcal{N}_P}(t) \\ &+ \Pi^{2\mathcal{N}_P\times 2\mathcal{N}_P} G^{2\mathcal{N}_P}(t)\end{aligned}$$

   from $t = \tau$ to $t = 0$.

7. The optimal control is given by

$$\overline{U}(t)^{2s}(t) = -\left(R^{2s\times 2s}\right)^{-1}\left(B^{2\mathcal{N}_P\times 2s}\right)^T\left[\Pi^{2\mathcal{N}_P\times 2\mathcal{N}_P}\hat{P}^{2\mathcal{N}_P\times 2\mathcal{N}} z^{2\mathcal{N}}(t) - r^{2\mathcal{N}_P}(t)\right] ,$$

   and the full order closed loop is given by

$$\begin{aligned}\dot{z}^{2\mathcal{N}}(t) &= \left[A^{2\mathcal{N}\times 2\mathcal{N}} - B^{2\mathcal{N}\times 2s}\left(R^{2s\times 2s}\right)^{-1}\left(B^{2\mathcal{N}_P\times 2s}\right)^T \Pi^{2\mathcal{N}_P\times 2\mathcal{N}_P}\hat{P}^{2\mathcal{N}_P\times 2\mathcal{N}}\right] z^{2\mathcal{N}}(t) \\ &+ B^{2\mathcal{N}\times s}\left(R^{s\times s}\right)^{-1}\left(B^{\mathcal{N}\times s}\right)^T r^{2\mathcal{N}_P}(t) + G^{2\mathcal{N}}(t) .\end{aligned}$$

6.1 LQR Control with Multiple Exogenous Frequency

In this example, we repeat the multiple exogenous frequency simulations presented in the previous section. The external exciting force is given by (14), (15) and (27), and we carry out simulations using $\mathcal{N}_P = 3, 6$ and 9 POD basis functions. The percentage of the full order model contained by the POD reduced order model is the same as Table 8 from the previous section. It can be seen from Table 8 and Figure 9 that the system is not resolved with $\mathcal{N}_P = 3$ POD functions ($N_P = 1$)and so we do not expect good attenuation with the control design based on this model when the reduced order gains are applied to the full order model. Figure 12 depicts that this is exactly the case. Control results in the longitudinal direction with $\mathcal{N}_P = 6$ and 9 POD functions ($N_P = 2, 3$) are shown in Figure 13, circumferential displacements are

in Figure 14 and transverse displacement are in Figure 15. The RMS plots of L_1 and L_2 are illustrated in Figures 16 and 17. As expected, the attenuation obtained is not as good as when the reduced order control is applied in the reduced order model. However, the overall effectiveness of the feedback control is still quite impressive.

Good attenuation using $\mathcal{N}_P = 12$ POD basis functions ($N_R = 12$) *was not* attained. Indeed, computations suggested great difficulty in stabilizing the system based on 12 POD element designs. An analysis of the controllability matrix $\mathcal{C}(A^{2\mathcal{N}_P}, B^{2\mathcal{N}_P})$ of the reduced order model using POD basis functions presented in Table 9 suggests a possible explanation. Its rank continues to decrease relative to the maximum possible rank until the system becomes significantly uncontrollable (as indicated by the controllability matrix rank deficit). Therefore as we increase N_P, the system becomes increasingly difficult to stabilize. Since feedback control in the reduced order model is already more difficult with 12 basis functions than with 9, then control in the full order model most likely is much more difficult.

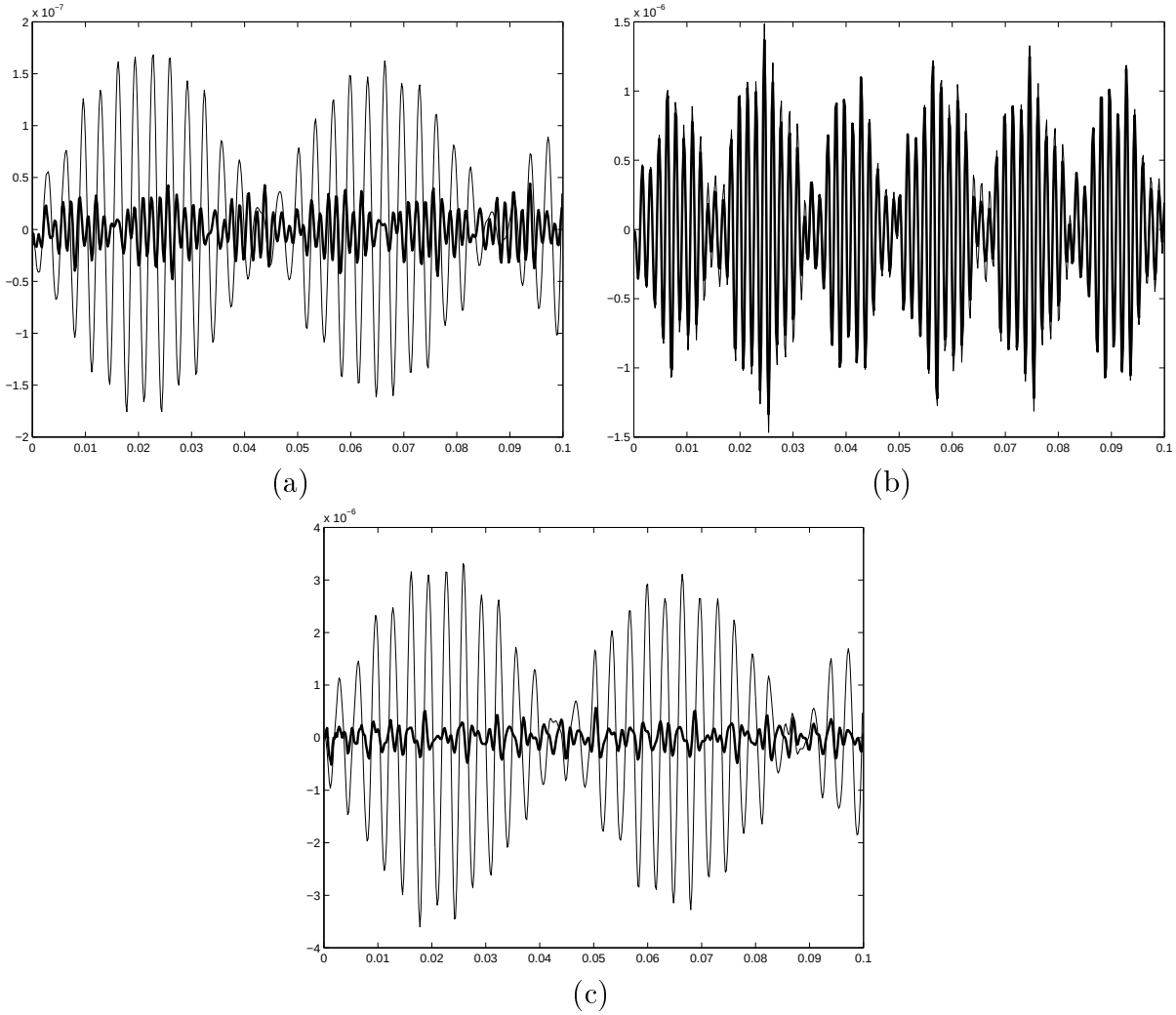

Figure 12. Full order uncontrolled and controlled shell displacements at the point p_1 with control design based on $\mathcal{N}_P = 3$ basis functions ($N_P = 1$); (a) longitudinal $u^{\mathcal{N}}(t, \hat{x}, \hat{\theta})$, (b) circumferential $v^{\mathcal{N}}(t, \hat{x}, \hat{\theta})$, (c) transverse $w^{\mathcal{N}}(t, \hat{x}, \hat{\theta})$; —— (uncontrolled), ▬▬ (controlled).

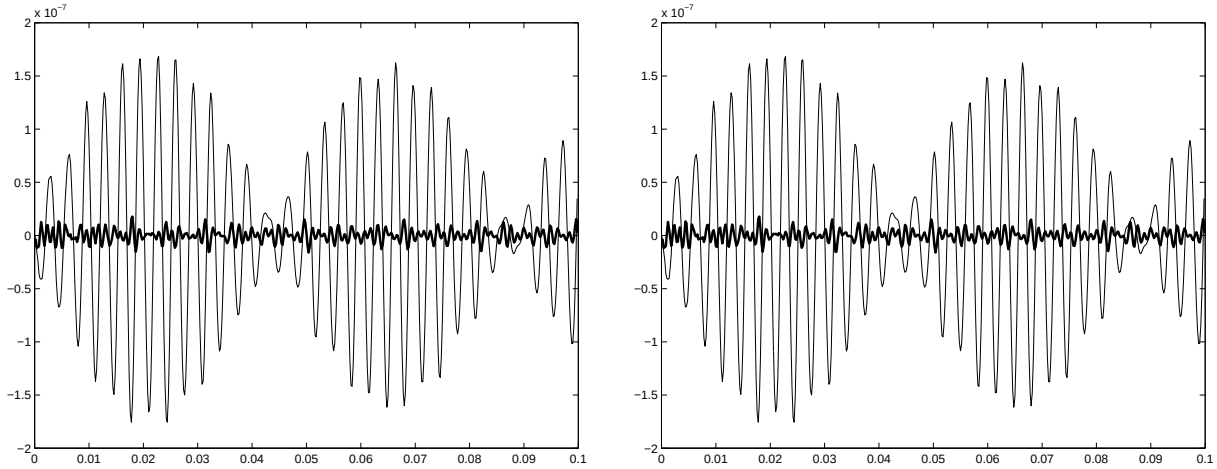

Figure 13. Full order uncontrolled and controlled displacements in the u direction at the point p_1 with control design based on (a) $\mathcal{N}_P = 6$ POD basis functions ($N_P = 2$), (b) $\mathcal{N}_P = 9$ POD basis functions ($N_P = 3$); —— (uncontrolled), ▬▬ (controlled).

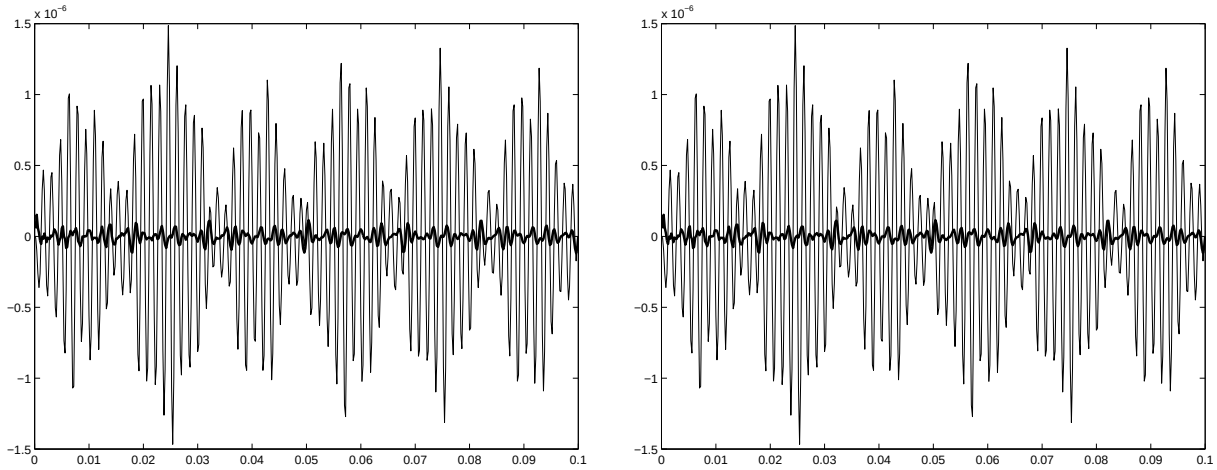

Figure 14. Full order uncontrolled and controlled displacements in the v direction at the point p_1 with control design based on (a) $\mathcal{N}_P = 6$ POD basis functions ($N_P = 2$), (b) $\mathcal{N}_P = 9$ POD basis functions ($N_P = 3$); —— (uncontrolled), ▬▬ (controlled).

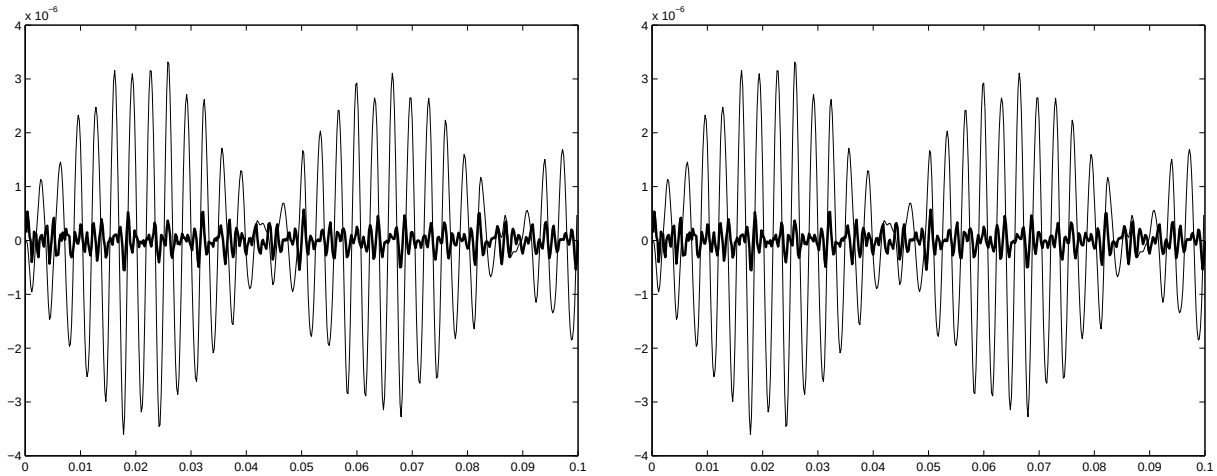

Figure 15. Full order uncontrolled and controlled displacements in the w direction at the point p_1 with control design based on (a) $\mathcal{N}_P = 6$ POD basis functions ($N_P = 2$), (b) $\mathcal{N}_P = 9$ POD basis functions ($N_P = 3$); —— (uncontrolled), ▬▬ (controlled).

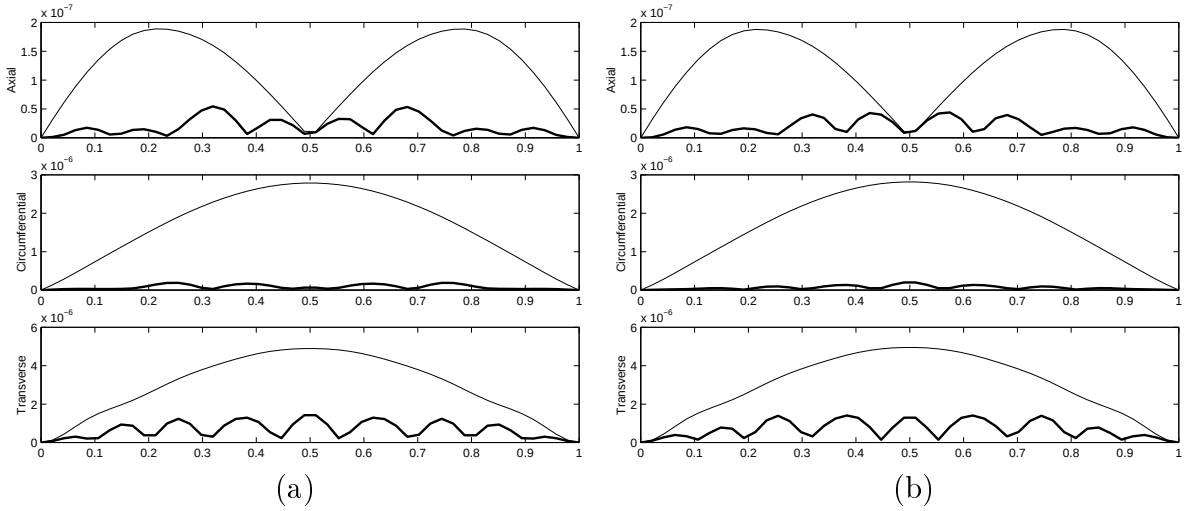

Figure 16. Full order uncontrolled and controlled root mean square displacements at the axial line L_1 with control design based on (a) $\mathcal{N}_P = 6$ POD basis functions ($N_P = 2$), (b) $\mathcal{N}_P = 9$ POD basis functions ($N_P = 3$); —— (uncontrolled), ▬▬ (controlled).

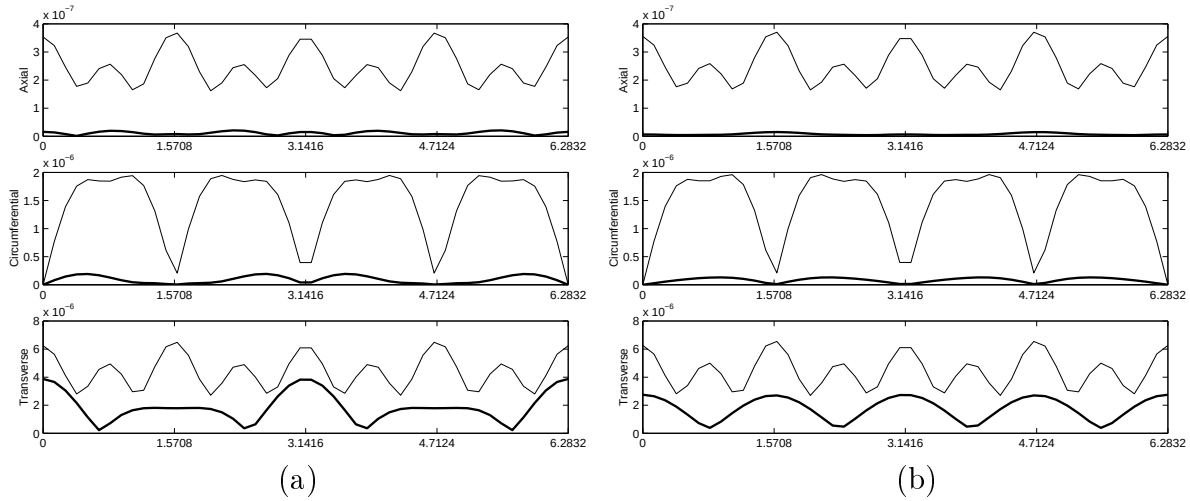

Figure 17. Full order uncontrolled and controlled root mean square displacements at the circumferential line L_2 with control design based on (a) $\mathcal{N}_P = 6$ POD basis functions ($N_P = 2$), (b) $\mathcal{N}_P = 9$ POD basis functions ($N_P = 3$); —— (uncontrolled), ▬▬ (controlled).

7 Concluding Remarks

Our preliminary computational investigations on the use of reduced order model based feedback control design suggest some positive features of such an approach. When they are effective, these designs can offer significant control authority with substantially reduced online computational requirements. Very low order designs (with cheap calculations) sufficed in some of the examples we tested. Both reduced basis methods (RBM) and proper orthogonal decomposition (POD) based methods can be effective, but both can lead one into difficulties. By their very nature, controllability deficiencies are inherent in both approaches and can in some cases render the methods useless. Increasing the order of approximation in the system can yield a badly uncontrollable system for which the design is destabilizing.

The RBM methods offer no systematic way to increase the level of approximation and ill-conditioning of system matrices can thwart efforts at increased accuracy in approximations. For the POD based methods, there is a systematic, optimal way to improve the level of approximation. Moreover, one can retain well-conditioned system matrices in doing this. In theory and in "textbook" examples (applying POD designed controllers to the POD system itself), the methods work well with increased order of approximation leading to improved results. However, in practice (use of POD based control designs on the full order model) controllability and stabilizability features (deficits) are worse as one increases the number of basis elements.

Our preliminary calculations suggest that reduced order model feedback control design ideas are worth pursuing. While they may prove quite adequate in some applications, there is still much to be learned. Our extensions of these ideas to compensator design and application to nonlinear system dynamics is currently underway but is in its infancy. It is too early to make a definite statement about the effectiveness of ROM design in general and POD design in particular in feedback control applications.

References

[1] B.O. Almroth, "Automatic choice of global shape functions in structural analysis," *AIAA Journal*, 16 (1978), pp. 525-528.

[2] H.T. Banks, R.C. Smith and Y. Wang, "The modeling of piezoceramic patch interactions with shells, plates, and beams," *Quarterly of Applied Mathematics*, 53 (1985), pp. 353-381.

[3] H.T. Banks, R.C. Smith and Y. Wang, "Modeling and parameter estimation for an imperfectly clamped plate," *Computation and Control IV,* (K.L. Bowers and J. Lund, eds.), Birkhäuser, Boston, 1995, pp. 23-42.

[4] H.T. Banks, R.C. Smith and Y. Wang, *Smart Material Structures: Modeling, Estimation and Control*, Masson/John Wiley, Paris/Chichester, 1996.

[5] H.T. Banks, M. Demetriou and R.C. Smith, "Utilization of coupling effects in compensator design for structural acoustic systems – numerical examples," *Journal of the Acoustical Society of America*, 103 (1998), pp. 872-887.

[6] H.T. Banks, R.C Smith, D. Brown, R. Silcox and V. Metcalf, "Experimental confirmation of a PDE-based approach to design of feedback controls," *SIAM Journal on Control and Optimization*, 35 (1997), pp. 1263-1296.

[7] G. Berkooz, P. Holmes, and J.L. Lumley, "The proper orthogonal decomposition in the analysis of turbulent flows," *Annual Review of Fluid Mechanics*, 25 (1993), pp. 539-575.

[8] W.L. Brogan, *Modern Control Theory*, Prentice Hall, New Jersey, 1991.

[9] R. del Rosario and R.C. Smith, "Spline approximation of thin shell dynamics," *International Journal for Numerical Methods in Engineering*, 40 (1997), pp. 2807-2840.

[10] R. del Rosario and R.C. Smith, "LQR control of shell vibrations via piezoceramic actuators," *International Series in Numerical Mathematics* (F. Kappel and K. Kunisch, eds.) Birkhäuser, Basel, 126 (1998), pp. 247-264.

[11] R. del Rosario and R.C. Smith, "LQR control of thin shell dynamics: formulation and numerical implementation," ICASE Report 97-59, 1997; *Journal of Intelligent Material Systems and Structures*, submitted.

[12] K. Ito and S.S. Ravindran, "A reduced order method for simulation and control of fluid flows, CRSC Technical Report CRSC-TR96-27, 1996; *Journal of Computational Physics*, submitted.

[13] K. Ito and S.S. Ravindran, "A reduced basis method for control problems governed by PDE", CRSC Technical Report CRSC-TR97-1, 1997; *International Series in Numerical Mathematics*, (F. Kappel and K. Kunisch, eds.), Birkhäuser, Basel, 1997.

[14] A.W. Leissa, *Vibration of Shells,* NASA SP-288, 1973; reprinted by the Acoustical Society of America through the American Institute of Physics, 1993.

[15] J.L. Lumley, "The structure of inhomogenous turbulent flows," *Atmospheric Turbulence and Wave Propagation* (A.M. Yaglom and V.I. Tatarski, eds.), Nanka, Moscow, 1967, pp. 166-178.

[16] H.V. Ly and H.T. Tran, "Proper orthogonal decomposition for flow calculations and optimal control in a horizontal CVD reactor," CRSC Technical Report 98-13, 1998; *Quarterly of Applied Mathematics*, submitted.

[17] D.A. Nagy, "Modal representation of geometrically nonlinear behavior by the finite element method," *Computers and Structures*, 10 (1979), pp. 683-688.

[18] A.K. Noor and J.M. Peters, "Reduced basis technique for nonlinear analysis of structures," *AIAA Journal*, 18 (1980), pp. 455-462.

[19] A.K. Noor, C.M. Andersen and J.M. Peters, "Reduced basis technique for collapse analysis of shells," *AIAA Journal*, 19 (1981), pp. 393-397.

[20] A.K. Noor, "Recent advances in reduction methods for nonlinear problems," *Computers and Structures*, 13 (1981), pp. 31-44.

[21] J.S. Peterson, "The reduced basis method for incompressible viscous flow calculations," *SIAM Journal on Scientific and Statistical Computing*, 10 (1989), pp. 777-786.